

# **Simulation Studies on Muon Neutrino DIS Analysis at the SND@LHC Detector**

Master's Thesis submitted

to

**Prof. Dr. Heiko Lacker**

Humboldt University of Berlin

Department of Physics

by

**Tilly Erin Smith**

632568

in partial fulfillment of the requirements

for the degree of

**Master of Science**

Berlin, 2025

## **Selbstständigkeitserklärung**

Ich erkläre hiermit, dass ich die vorliegende Arbeit selbstständig verfasst und noch nicht für andere Prüfungen eingereicht habe. Sämtliche Quellen einschließlich Internetquellen, die unverändert oder abgewandelt wiedergegeben werden, insbesondere Quellen für Texte, Grafiken, Tabellen, Bilder sowie die Nutzung von Künstlicher Intelligenz für die Erstellung von Texten und Abbildungen, sind als solche kenntlich gemacht. Mir ist bekannt, dass bei Verstößen gegen diese Grundsätze ein Verfahren wegen Täuschungsversuchs bzw. Täuschung eingeleitet wird.

Berlin, September 30, 2025, .....

I hereby confirm that I have authored this Master's thesis independently and without use of others than the indicated sources. All passages which are literally or in general matter taken out of publications or other sources are marked as such.

Berlin, September 30, 2025, .....

## Abstract

The importance of neutrinos at the scattering neutrino detector (SND) for tests of the standard model (SM) and for the search of physics beyond the standard model (BSM) is the motivation of this work. As of now 8  $\nu_\mu$  candidates have been found at SND, corresponding to a selection efficiency of  $\approx 3\%$ . The following work aims to increase this efficiency through the spatial analysis of  $\nu_\mu$  charged-current (CC) deep inelastic scattering (DIS) events and relevant background processes in the muon system of the detector using Monte Carlo (MC) data.

For this definitions are presented for the characterization of the signature outgoing muon and hadron shower of a  $\nu_\mu$ -CC DIS event. Through this, a set of parameters is identified that show significant discrimination power between signal and background processes. These highlight the importance of the SciFi system over the muon system for signal extraction. Next, the parameters are taken advantage of as a basis for several classification methods: two likelihood-based methods and a gradient boosted decision tree (BDT). The neutral hadron background (NHB) mimicking signal behavior and the dominating presence of the passing muon background (PMB) are the biggest challenges to overcome in this procedure. However, the feasibility of all classification methods is proven but future studies are necessary to create a fully realized classification strategy out of the methods presented here. A lack of MC statistics limits the performance evaluation but could be addressed with additional resources. Finally, a comparison with experimental data is performed but inconclusive due to the lack of data available. The comparison is nevertheless valuable and gives insight into the detector behavior and potential flaws of the simulation studies.

Overall, the work successfully demonstrates the signal discrimination power of both the muon system and the SciFi system. A set of parameters is identified and utilized as a basis for classification methods, whose preliminary efficiencies promise to match or surpass those of previous  $\nu_\mu$  selection strategies.

## Zusammenfassung

Die Relevanz von Neutrinos beim "Scattering Neutrino Detector" (SND) als Test des Standardmodells (SM) und für die Suche für Physik jenseits des Standardmodells (BSM) ist die Motivation dieser Arbeit. Zum Zeitpunkt dieser Arbeit wurden im SND Bis 8  $\nu_\mu$  Kandidaten gefunden im SND. Daraus ergibt sich eine Selektionseffizienz von 3%. Ziel der vorliegenden Arbeit ist es die Effizienz durch die räumliche Analyse von  $\nu_\mu$  schwach wechselwirkende (CC) und tief inelastisch streuende (DIS) Ereignissen zu erhöhen. Ebenso werden relevante Hintergrundprozesse im Muonsystem des SND mithilfe von Monte Carlo Daten zur Effizienzsteigerung herangezogen.

Definitionen für die Charakterisierung der ausgehenden Myonen und Hadronenschauer der  $\nu_\mu$ -CC DIS Ereignisse vorgestellt. Es werden Parameter identifiziert die eine hohe Diskriminierungs zwischen Signal und Hintergrundprozesse aufweisen. Für die Bestimmung von Signal Ereignissen ergibt sich eine gestiegerte Bedeutung des SciFi Systems im Vergleich zum Muonsystem. Danach werden die Parameter als Basis für einige Klassifizierungsmethoden verwendet: zwei Likelihood-basierte Analysemethoden und ein gradient boosted decision tree (BDT). Die größte Herausforderung in diesem Prozess ist das Nachahmen des neutralen Hadronenhintergrund (NHB) des Signals und die Dominanz der Präsenz des durchlaufenden Myon-Hintergrund (PMB). Nichtsdestotrotz ist die Realisierbarkeit der Klassifizierungsmethoden bewiesen. Es sind jedoch weitere Studien notwendig um eine allumfassende Klassifizierungsmethode aus den hier präsentierten Methoden zu realisieren. Ein Mangel an Daten limitiert die Leistungsbewertung, kann aber mit weiteren Mitteln beseitigt werden. Die letztendlich vorgenommene Gegenüberstellung mit experimentellen Daten ist aufgrund mangelnder Daten jedoch nicht eindeutig. Diese Gegenüberstellung ist aber trotzdem relevant, da sie einen wichtigen Einblick in das Verhalten des Detektors und potentielle Fehler der Simulationstudie aufzeigt.

Insgesamt demonstriert die hier präsentierte Arbeit erfolgreich die Diskriminierungskraft der Myonen- und SciFi-Systeme. Es wurden eine Vielzahl von Parametern identifiziert, die als weitere Basis für Klassifizierungsmethoden dienen. Dessen vorläufige Effizienz ist vergleichbar oder sogar besser ist als die vorangegangenen  $\nu_\mu$ -CC DIS Selektionsstrategien.

# Contents

<b>1</b>	<b>Introduction</b>	<b>1</b>
<b>2</b>	<b>Detector and Experimental Setup</b>	<b>3</b>
<b>3</b>	<b>Simulation and Reconstruction</b>	<b>5</b>
3.1	General Configuration . . . . .	5
3.2	Monte Carlo Data Samples . . . . .	5
3.2.1	MC Simulation Datasets . . . . .	5
3.2.2	Normalization Procedure . . . . .	6
3.3	Event Selection Cuts . . . . .	8
3.4	Shower Reconstruction . . . . .	13
3.5	Muon Reconstruction . . . . .	23
3.6	Summary . . . . .	30
<b>4</b>	<b>Classification Strategies</b>	<b>32</b>
4.1	Likelihood-based Methods . . . . .	32
4.1.1	Likelihood Ratio Test . . . . .	32
4.1.2	Construction of Likelihood Fits . . . . .	38
4.2	Boosted Decision Tree (BDT) Analysis . . . . .	41
4.3	Summary . . . . .	50
<b>5</b>	<b>Comparison with Run Data</b>	<b>51</b>
<b>6</b>	<b>Conclusions and Outlook</b>	<b>57</b>
<b>References</b>		<b>60</b>
<b>List of Abbreviations</b>		<b>62</b>
<b>List of Figures</b>		<b>62</b>
<b>List of Tables</b>		<b>64</b>
<b>A Figures</b>		<b>65</b>

# 1 Introduction

The scattering neutrino detector at LHC (SND@LHC) is a compact, standalone experiment located 480 m downstream of the ATLAS interaction point in the TI18 tunnel, as can be seen in Fig. 1. Proton-proton (pp) collisions with a center-of-mass energy of 13.6 TeV at LHC produce a large neutrino flux through leptonic W, Z, b and c decays, which are further increased through ensuing pion and kaon decays. The high-intensity beam of  $O(7 \times 10^{12})$  neutrinos can be taken advantage of in this experiment by positioning SND in a rapidity region of  $7.2 < \eta < 8.4$ .

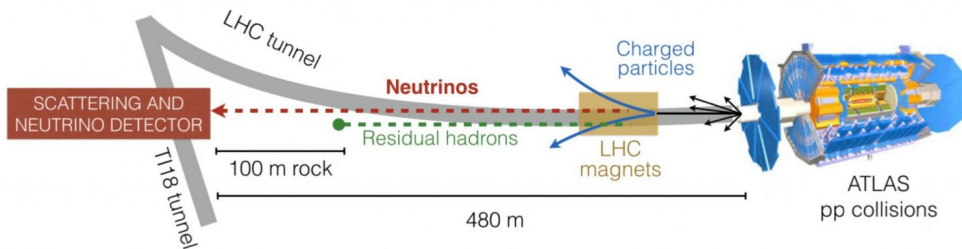


**Figure 1:** Location of SND@LHC, it can be found in the TI18 tunnel, 480m downstream of the ATLAS interaction point. A large neutrino flux, resulting from pp collisions at LHC, propagates in the far forward direction and arrives at the SND experiment. [1]

SND is designed to detect and perform analysis on all three neutrino flavors, enabling direct insight into heavy-flavor productions by measuring the neutrino flux and cross sections. Additionally, current cross-section measurements are extended to a previously unexplored energy region of 350 GeV to 10 TeV as can be seen in Fig. 2. This experiment was approved in 2021 and installed in 2022, where it has taken an integrated luminosity of  $68.6 \text{ fb}^{-1}$  data since and is expected to take  $250 \text{ fb}^{-1}$  of data during the entirety of Run3. Analysis has been performed on  $36.8 \text{ fb}^{-1}$  of this and 8 muon neutrino  $\nu_\mu$  charged current (CC) deep inelastic scattering (DIS) candidates have been found with a significance of  $7\sigma$  (see [2]).

Some of the main goals of the neutrino analysis are to study the charmed hadron production from pp collisions through the large fraction of neutrinos resulting from these decays, test the lepton flavor universality (LFU) and measure the neutral current (NC)/CC ratio. However, the focus of this thesis is the replication of the  $\nu_\mu$ -CC DIS and the corresponding characteristic outgoing muon and hadron shower (see Fig. 3) using Monte Carlo (MC) data. Significant background processes that could mimic a signal interaction vertex are included

in this work, such as: passing muons producing electromagnetic showers, muon DIS and a neutral background produced by muons scattering in the cavern rock upstream of SND.

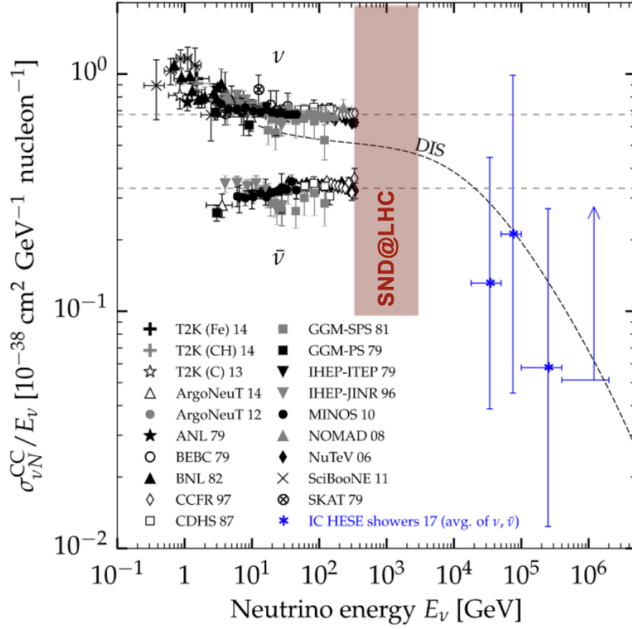


**Figure 2:** Current cross-section measurements from different experiments over the neutrino energy  $E_\nu$ . Highlighted in red is the previously unexplored energy range being probed by SND@LHC. [3]

In this simulation study, the aim is to achieve a comparable or higher signal-background ratio than previous analysis studies and thus increase the amount of identified  $\nu_\mu$ -CC DIS events. For this the spatial development of the relevant processes is characterized and compared, to subsequently find discriminating parameters between signal and background.

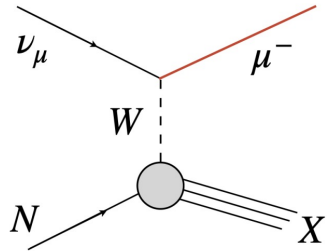


**Figure 3:** Feynman diagram for the  $\nu_\mu$ -CC DIS process on a target nucleon N, here an outgoing muon  $\mu^-$  (red) and hadron shower X are the expected signature. [2]

Furthermore, certain components of the simulation study are compared with experimental data to evaluate the methods developed and also to give insight into the detector performance.

In this thesis, the detector setup and concept will first be described. After that an overview of the simulation study is given, including: normalization of the MC data, selection cuts performed and the spatial characterization and development of the  $\nu_\mu$ -CC DIS. Finally, a series of analysis methods - two likelihood based classification methods and a gradient BDT - the comparison with run data and a discussion of the results follow.

## 2 Detector and Experimental Setup

In this chapter a quick overview of the design and setup of the detector is given, for further details see [4]. SND is comprised of three subsystems: the veto system, target system and muon system; the detector dimensions are  $0.6\text{ m} \times 0.8\text{ m} \times 2.6\text{ m}$ . A right-handed coordinate system is used throughout with z aligned along the collision axis, y vertically and x horizontally aligned with the detector as can be seen in Fig. 4.

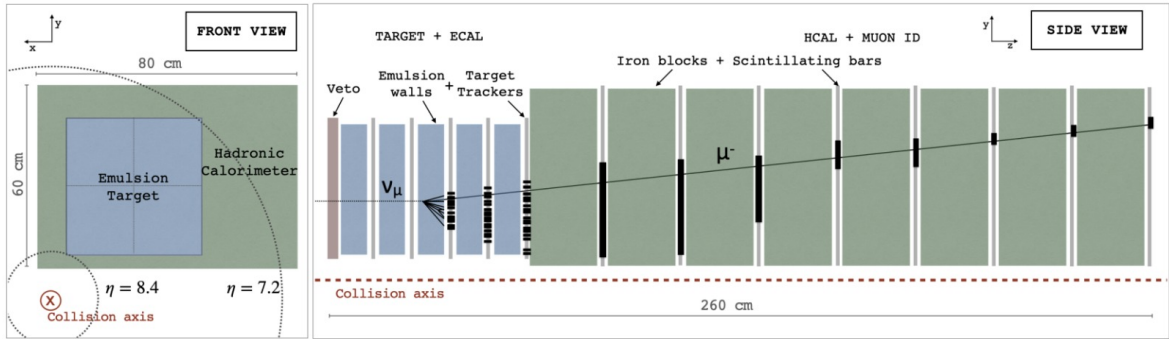


**Figure 4:** Schematic diagram of the SND detector in front (left) and side view (right). This is comprised of the veto system, target detector and ECAL and the HCAL and muon system. Furthermore, an example of a  $\nu_\mu$ -CC DIS interaction is depicted in the side view. [2]

The first subsystem, the veto system, aims to tag charged particles entering the detector and veto these to suppress charged background. The veto system is made up of two planes of seven scintillating bars ( $1 \times 6 \times 42\text{ cm}^3$ ) each with a separation of 4.2 cm. The bars are read out on either side by eight silicon photomultipliers (SiPMs) placed on a common printed circuit board (PCB) and wrapped in aluminum foil to ensure light tightness. About  $10^4$  photons are created by a minimum-ionising particle (MIP) crossing 1 cm of the scintillating bars. The inefficiency of the two veto planes has been calculated to be  $4.5 \times 10^{-4}$  during the period where  $36.8\text{ fb}^{-1}$  were taken [2]. In some cases the first two SciFi stations of the target system are included in the veto process, these have an inefficiency of  $1.1 \times 10^{-4}$  each,

resulting in a total inefficiency for this extended veto system of  $5.3 \times 10^{-12}$ .

Secondly, the target system consists of five walls, each containing a layer of four emulsion bricks followed by a SciFi tracker station. The five SciFi stations make up the ECAL. The target material used is tungsten and can be found as 59 1 mm thick layers in the emulsion bricks, interchanging with emulsion films according to the emulsion cloud chamber (ECC) technique as in Fig. 5. This brings the thickness of a brick to 78 mm, corresponding to  $17X_0$ ; the transverse area of each brick wall is  $192 \times 192$  mm $^2$ . In this way a target weight of 830 kg and sub-micrometric positional resolution is achieved. The SciFi stations of the ECAL consist of two layers, one in x and one in y view. Each station is made up of six densely packed scintillating fibers, read out by eight SiPMs on each side. The resolution of these SciFi trackers is 150  $\mu\text{m}$  and 250 ps for a particle crossing both x and y layers. Combined, the ECAL, target and emulsion allow for efficient tracking of charged particles entering the system and for a precise vertex recreation.

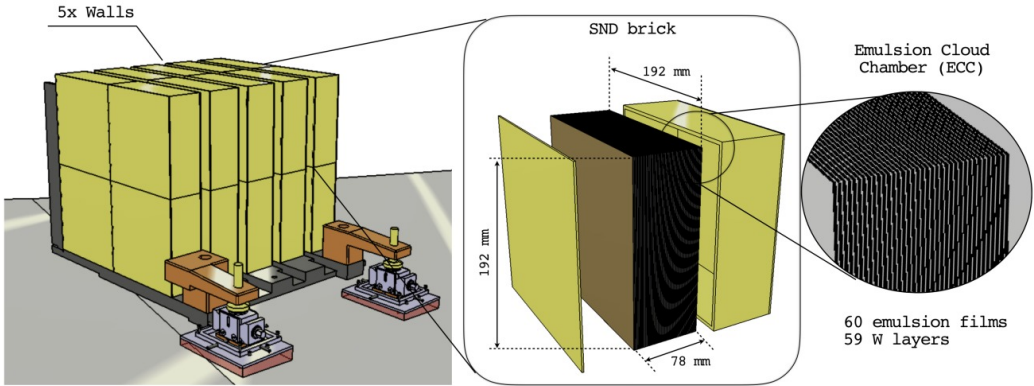


**Figure 5:** Depicted is the ECC technique used in the target walls, where the thin layers of the target material - tungsten - alternate with emulsion films. [4]

Finally, the muon system and HCAL have the goal of identifying and reconstructing the outgoing muon characteristic for a  $\nu_\mu$ -CC DIS interaction. This is made up of eight stations, consisting of scintillating planes interchanging with 20 cm thick iron slabs acting as passive material, achieving  $9.5 \cdot \lambda_{int}$  and a time resolution of 120 ps. The five upstream (US) most stations have ten horizontally stacked scintillating bars with  $81 \times 6 \times 1$  cm $^3$ , read out by eight SiPMs on each side. This results in an active area of  $81 \times 60$  cm $^2$  per layer. The last three downstream (DS) stations are made up of two layers of 60 scintillating bars each, one stacked horizontally and the other vertically. Here, each bar is read out by one SiPM on each side and the spatial resolution reaches less than 1 cm.

## 3 Simulation and Reconstruction

In this section an overview of the developed simulation is given by first presenting the general configuration of the experiment. Next, the MC data used for all processes and how they are produced is presented along with the corresponding normalization. A series of selection cuts is introduced, aiming to extract signal events from the underlying background processes. Finally the methods for reconstructing the  $\nu_\mu$ -CC DIS interaction vertex, hadron shower and the characteristic outgoing muon are presented.

### 3.1 General Configuration

In this work the experiment configuration of 2022 and corresponding data taken during that period is simulated. This corresponds to an integrated luminosity of  $L = 36.8 \text{ fb}^{-1}$ ,  $8.3 \cdot 10^9$  events, an average target mass of 792 kg and a downward beam crossing angle of  $-160 \mu\text{rad}$ . With the given target weight, a signal yield of  $157 \pm 37$   $\nu_\mu$ -CC DIS is expected in this configuration in the target [2]. As mentioned in the introduction, the background processes considered in this work are a passing muon background (PMB) producing electromagnetic showers, muon DIS in the detector and additionally muons scattering upstream of the detector in the tunnel rock, producing a neutral hadron background (NHB). The passing muon flux was measured to be  $(2.07 \pm 0.01 \text{ (stat)} \pm 0.10 \text{ (sys)}) \cdot 10^4 \text{ cm}^2/\text{fb}^{-1}$  in a defined fiducial area of  $25 \cdot 26 \text{ cm}^2$  [2], [5]. This results in a total number of muons of  $5.0 \cdot 10^8$  in the detector for  $36.8 \text{ fb}^{-1}$ . The corresponding muon DIS rate in the target is  $4.5 \cdot 10^4/\text{fb}^{-1}$ , yielding  $1.65 \cdot 10^6$  interactions for  $36.8 \text{ fb}^{-1}$ . Finally, the neutral background yield due to kaons and neutrons is expected to be  $8.61 \cdot 10^4$  within the detector [2].

### 3.2 Monte Carlo Data Samples

In the following chapter the production of the MC files used within this work is described and the necessary normalization to  $36.8 \text{ fb}^{-1}$  for signal and background processes is presented.

#### 3.2.1 MC Simulation Datasets

Throughout the SND@LHC experiment the pp collisions and event generation at ATLAS IP1 are simulated using the FLUKA code [6] with the Dual Parton Model including charm (DPMJET3). Subsequently, FLUKA propagates the resulting particles towards the detector and simulates the production of neutrinos from decays of long-lived particles as well as neutrino production due to re-interaction of particles with the surrounding material. Similarly,

the PMB is simulated by FLUKA in this way via pions and kaons decaying on their way towards the detector until they are recorded at a scoring plane ( $1.8 \times 1.8 \text{ m}^2$ ) 60 m upstream of SND. The further transportation of neutrinos and the PMB through the TI18 tunnel and SND is done with GEANT4 [7], including interactions along the way with the detector surroundings such as muon DIS. GENIE is used for the simulation of  $\nu_\mu$ -CC DIS with the detector material in SND [8]. With the muon spectrum obtained at the detector from FLUKA, the NHB can be simulated using PYTHIA [9] by considering scattering of  $\mu^-/\mu^+$  on at rest protons and neutrons. The secondary particles are placed along the muon flight path and the transportation through SND is achieved with GEANT4; the QGSP\_BERT\_HP\_PEN physics list is utilized.

### 3.2.2 Normalization Procedure

The normalization to a desired luminosity of  $36.8\text{fb}^{-1}$  for this work varies depending on the process of interest due to differing file structures. The  $\nu_\mu$ -CC DIS files are pre-scaled to a luminosity of  $100\text{fb}^{-1}$ . FLUKA event weights  $w_{\text{event}}$ , scaling the simulated events to their physical expected occurrences, are also already included. To rescale these files to  $36.8\text{fb}^{-1}$  a final scaling factor  $w_{\nu_\mu}$  is applied

$$w_{\nu_\mu} = \frac{36.8\text{fb}^{-1}}{100\text{fb}^{-1} \cdot N_{\text{files}}}, \quad (1)$$

where  $N_{\text{files}}$  is the amount of files used from this simulation sample. Similarly, the PMB is scaled to the desired luminosity taking into account the amount of files used and the luminosity  $L_{\text{PMB}}$  of the given files. The latter has to first be calculated using the number of pp collisions  $N_{\text{coll}}$  and the inclusive pp cross-section  $\sigma_{\text{pp}}$ , giving the final scaling factor

$$w_{\text{PMB}} = \frac{36.8\text{fb}^{-1}}{L_{\text{PMB}} \cdot N_{\text{files}}} \cdot w_{\text{event}}, \quad (2a)$$

$$\text{with } L_{\text{PMB}} = \frac{N_{\text{coll}}}{\sigma_{\text{pp}}} = \frac{78 \cdot 10^6}{78.1\text{mb}} \approx 1 \cdot 10^{-6}\text{fb}^{-1}. \quad (2b)$$

Now also including the FLUKA event weights  $w_{\text{event}}$ . To normalize the muon DIS background a different procedure is necessary. The scaling factor  $w_{\text{muonDIS}}$  is comprised of three parts:

$$w_{\text{muonDIS}} = w_{\text{LHC}} \cdot w_{\text{muon}} \cdot n_{\text{file}} \cdot 36.8, \quad (3a)$$

$$\text{with } w_{\text{LHC}} = \frac{N_{\text{event}}}{2 \cdot 10^8 \cdot 10 \cdot 2} = \frac{R}{2 \cdot 10^8} \cdot \frac{w_{\text{event}}}{10 \cdot 2} \cdot 10^5 \text{s}, \quad (3b)$$

$$w_{\text{muon}} = \chi \cdot w_{\text{DIS}} = \chi \cdot 0.6 \cdot 10^{-3} \cdot \sigma_{\text{DIS}}. \quad (3c)$$

First, the weight  $w_{\text{LHC}}$  scales the FLUKA generated muons to LHC conditions by taking into account the number of events  $N_{\text{event}}$  for an integrated luminosity of  $L = 1 \text{ fb}^{-1}$ , the amount of muons generated by the FLUKA team  $2 \cdot 10^8$ , the correction factor 2 because the same flux was used to generate DIS on both neutrons and protons and the correction factor 10 because the same muon was generated 10 times to increase statistics. Where  $N_{\text{event}}$  is obtained by multiplying the pp interaction rate  $R = L_{\text{inst}} \cdot \sigma_{\text{pp}} = 10^{34} \text{ cm}^{-2} \text{ s}^{-1} \cdot 78.1 \text{ mb} \approx 8 \cdot 10^8 \text{ s}^{-1}$  (where  $L_{\text{inst}}$  is the instantaneous luminosity), the FLUKA event weight  $w_{\text{event}}$  of the primary muon and the time window of  $10^5 \text{ s}$ . Second, the factor  $w_{\text{muon}}$  represents the amount of muon DIS interactions occurring along the primary muon's trajectory. This is obtained by multiplying the density along the muon trajectory  $\chi$  with the probability of a muon DIS interaction  $w_{\text{DIS}}$ . Finally, the fraction of files  $n_{\text{file}}$  used from the simulated dataset and the desired integrated luminosity of  $36.8 \text{ fb}^{-1}$  are multiplied, resulting in the final scaling factor  $w_{\text{muonDIS}}$  in eq. 3a for the muon DIS background.

Energy [GeV]	Neutrons			Kaons		
	Interaction Rate	Particles Generated	Yield	Interaction Rate	Particles Generated	Yield
5–10	$4.62 \cdot 10^4$	$2.12 \cdot 10^6$	0	$2.51 \cdot 10^4$	$2.14 \cdot 10^6$	0
10–20	$7.59 \cdot 10^3$	$2.05 \cdot 10^6$	$3.70 \cdot 10^{-3}$	$5.72 \cdot 10^3$	$2.09 \cdot 10^6$	$1.91 \cdot 10^{-2}$
20–30	$1.18 \cdot 10^3$	$7.54 \cdot 10^5$	$4.69 \cdot 10^{-3}$	$8.53 \cdot 10^2$	$7.49 \cdot 10^5$	$2.28 \cdot 10^{-3}$
30–40	$5.30 \cdot 10^2$	$7.41 \cdot 10^5$	$3.58 \cdot 10^{-3}$	$1.10 \cdot 10^2$	$7.53 \cdot 10^5$	$1.17 \cdot 10^{-3}$
40–50	$4.66 \cdot 10^2$	$7.37 \cdot 10^4$	$6.33 \cdot 10^{-3}$	$9.38 \cdot 10^1$	$7.43 \cdot 10^5$	$1.64 \cdot 10^{-3}$
50–60	$2.60 \cdot 10^1$	$3.35 \cdot 10^5$	$3.10 \cdot 10^{-4}$	$6.48 \cdot 10^1$	$3.41 \cdot 10^5$	$2.28 \cdot 10^{-3}$
60–70	$1.80 \cdot 10^1$	$3.33 \cdot 10^5$	$7.10 \cdot 10^{-4}$	$9.90 \cdot 10^0$	$3.34 \cdot 10^5$	$2.07 \cdot 10^{-4}$
70–80	$8.48 \cdot 10^0$	$3.24 \cdot 10^5$	$3.66 \cdot 10^{-4}$	$2.32 \cdot 10^1$	$3.35 \cdot 10^5$	$4.84 \cdot 10^{-4}$
80–90	$8.48 \cdot 10^0$	$1.17 \cdot 10^5$	$3.61 \cdot 10^{-4}$	$1.15 \cdot 10^1$	$3.17 \cdot 10^5$	$5.44 \cdot 10^{-4}$

**Table 1:** Interaction rates, generated particles, and yields for neutrons and kaons in various energy ranges. Data shown for  $L = 36.8 \text{ fb}^{-1}$  using the QGSP\_BERT\_HP\_PEN physics list [2].

The procedure for NHB is again somewhat different. Simulated NHB datasets are used to obtain the expected interaction rate in the SND target in absence of veto hits, this can be

found in Table 1 for both neutrons (left) and kaons (right) for  $36.8\text{fb}^{-1}$ .

However, this is computationally very expensive and only a small number of events can be generated. To circumvent this limitation the NHB events can instead be generated using a particle gun; this approach allows the creation of sufficient statistics. A correction is applied to account for the double counting of the veto. Finally, the NHB files produced in this way can be scaled to the expected interaction rate per energy range  $i$  as follows:

$$(w_{\text{NHB}})_i = \left( \frac{R}{N_{\text{gen}} \cdot n_{\text{file}}} \right)_i. \quad (4)$$

Where  $R$  is the interaction rate,  $N_{\text{gen}}$  is the amount of generated particles and  $n_{\text{file}}$  is the fraction of files used from that simulated dataset. It is also possible to scale the NHB to the expected yield  $Y$  by substituting this with  $R$  in eq. 4.

### 3.3 Event Selection Cuts

After obtaining the necessary MC files and normalizing these to the desired integrated luminosity of  $36.8\text{fb}^{-1}$ , a series of selection cuts is applied. These cuts are tailored to the selection of  $\nu_\mu$ -CC DIS interactions and the suppression of the background processes. An overview of the cuts, along with the corresponding efficiencies  $\frac{\text{cut}_j}{\text{cut}_i}$  ( $j > i$  and  $i, j \in [1, 17]$ ) can be found in Table 2 for the signal and background processes. As stated previously, one of the goals of this work is to find possible relaxations in these selection cuts through the spatial analysis performed in later chapters.

The selection cuts used here can be grouped into four categories: pre-selection cuts, fiducial cuts, veto cuts and neutrino selection cuts; these are based on the analysis cuts performed in [2]. First, pre-selection cuts are applied to mimic the detector energy deposition threshold in both the SciFi (22 keV per channel) and the HCAL (1 MeV per bar). Both of these cuts have an efficiency close to 1.0, meaning almost no events are rejected, but nevertheless these cuts are essential to reject hits with a low energy deposition that wouldn't be picked up by the detector. A fiducial cut is put into place, ensuring the reconstruction of the entire interaction within the detector volume and excluding the edge of the detector. For this the average SciFi channel per event is required to be within [200, 1200] in vertical projection and [300, 1336] for the horizontal projection. Similarly, the average DS bar per event must be within [10, 50] vertical and [70, 105] horizontal; in total a fiducial area of  $25 \times 26\text{cm}^2$  is established. When comparing the SciFi fiducial efficiencies of the signal and background processes, a large variation of up to 45% can be observed.

Cut applied	$\nu_\mu$ -CC DIS Efficiency	PMB Efficiency	Muon DIS Efficiency	NHB Efficiency
<b>Preselection Cuts</b>				
1.) SciFi ch. energy threshold (22keV)	0.999	0.999	0.999	0.999
2.) HCAL bar energy threshold (1MeV)	0.997	0.967	0.993	0.947
<b>Fiducial Cuts</b>				
3.) Avg. SciFi ch.: [200,1200] vertical, [300,1336] horizontal	0.560	0.081	0.121	0.605
4.) Avg. DS bar: [10,50] vertical, [70,105] horizontal	0.808	0.856	0.755	0.980
<b>Extended Veto Cuts</b>				
5.) No veto hits	0.579	0.010	0.049	0.244
6.) No hits in 1st SciFi station	0.854	0.822	0.859	0.750
7.) No hits in 2nd SciFi station	0.721	0.633	0.795	0.604
<b><math>\nu_\mu</math>-CC DIS Selection Cuts</b>				
8.) Interaction vertex not in 5th target wall	0.568	0.605	0.589	0.782
9.) $\geq 2$ consecutive SciFi stations hits	0.984	0.261	0.689	0.901
10.) If DS hit, then require hits in all US planes	0.996	0.833	0.978	0.997
11.) Reconstructed muon track	0.504	0.200	0.041	0.001
12.) Latest DS hit $t >$ earliest SciFi hit $t$	1.000	1.000	1.000	1.000
13.) Track intersects 1st SciFi station $\geq 5\text{cm}$ away from detector edge	0.671	-	0.167	0.444
14.) Sum of min(DOCA) to SciFi hits $< 3\text{cm}$	0.784	-	-	0.250
15.) More than 35 SciFi hits	0.918	-	-	1.000
16.) US $\sum QDC \geq 700$	0.701	-	-	1.000
17.) $< 10$ DS hits per projection	0.786	-	-	1.000
<b>Total efficiency</b>	0.03	0.0	0.0	0.008

**Table 2:** Cutflow of the applied selection cuts along with the corresponding efficiencies  $\frac{\text{cut}_j}{\text{cut}_i}$  ( $j > i$  and  $i, j \in [1, 17]$ ) per process. The cuts can be grouped into four categories from top to bottom: pre-selection cuts, fiducial volume cuts, extended veto cuts and  $\nu_\mu$ -CC DIS selection cuts.

An explanation can be found when looking at the distribution of the average SciFi channels for these processes, Fig. 6. The fired SciFi channels of the signal are roughly uniformly spread over the designated SciFi volume because the signal MC files are forced to perform interactions in the target walls. The method of creating the NHB using particle guns also allows for a uniform distribution of this background process over the entire SciFi area, leading to a SciFi cut efficiency equal to the ratio of the fiducial area to the sensitive SciFi area. For the muon DIS and PMB no such restraints are applied before this cut is performed and certain hot-spots can be found outside the fiducial area, leading to a smaller cut efficiency.

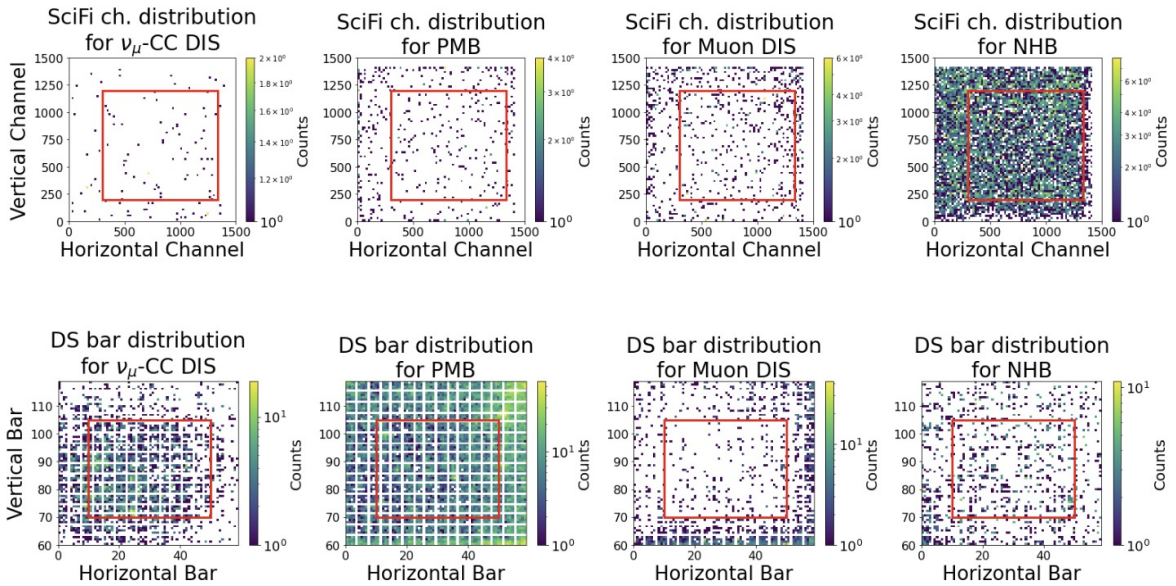


**Figure 6:** Distribution of hit SciFi channels (top) and DS bars (bottom) pre fiducial cuts, the fiducial area is highlighted in red.

Veto cuts are applied by excluding events where the veto fires. The veto cut (Cut 5) is identified as having the largest overall contribution to suppressing the background processes, emphasized by the discrepancy in this cut efficiency between signal (57.9%) and the background ( $\approx 1 - 25\%$ ). Optionally, the first two SciFi planes can be added to increase the veto performance, called the extended veto. In this work the extended veto is initially applied and the veto inefficiencies listed in the detector setup (chapter ??) are implemented. Again, the efficiency of the initial veto cut varies greatly between the different processes. This is to be expected due to the different charges of particles involved; the charged muons and secondary particles in the PMB and muon DIS lead to smaller veto efficiencies. Contrarily, the efficiencies of the extended veto are comparable between the different processes at around 82% for

the first SciFi station and 69% for the second SciFi station. Indicating, that the first two SciFi planes don't add significant discriminating power between signal and background while nevertheless reducing the statistics. This is highlighted by the relative statistics left after the veto cuts compared to initial statistics: 25% for the signal, 0.06% for the PMB, 0.45% for the muonDIS and 13% for the NHB. Here the signal efficiency is  $\approx 12 - 24\%$  larger than the background processes. Comparing this with the relative statistics after the extended veto cuts - 15.78% for signal, 0.03% for PMB, 0.3% for muon DIS and 6.26% for NHB - confirms that the signal efficiency is only  $\approx 9 - 14\%$  larger than for the background processes. It is thus recommended to only implement the initial veto plane in future data cuts to retain larger statistics and instead use the full SciFi system for analysis.

Finally, the  $\nu_\mu$  selection cuts are applied, where further analysis in later chapters show that the spatial development of events in the HCAL can be taken advantage of to relax these cuts (see chapter 6). The selection cut criteria vary depending on the specific analysis goals. For example, some cuts ensure a clean, well-contained signal with sufficient time and space to develop (Cuts 8, 10, 12, 13, 14, 17). While others are designed to separate the signal from the background processes and require significant activity in the SciFi and US (Cuts 9, 11, 15, 16). Some of the cuts implemented make use of the reconstructed muon track, which will be explained in detail in chapter 3.5. The QDC (Charge-to-Digital Converter) value found in cut 16 is calculated from the MC energy deposition using the conversion factor:  $QDC = E_{loss,MC} \cdot 25000$ , where  $E_{loss,MC}$  is the energy deposition per MC point.

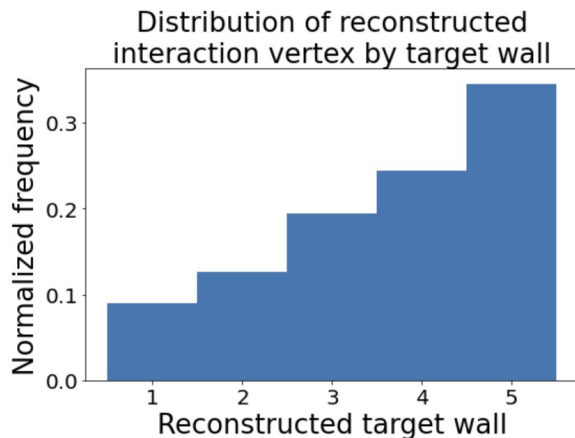


**Figure 7:** A shower wall tagging algorithm uses the relative hit density found in the SciFi stations to reconstruct the primary interaction vertex of the  $\nu_\mu$ -CC DIS. Depicted is the distribution of the resulting interaction vertices by target wall.

Furthermore, to locate the primary interaction vertex (Cut 8) a shower wall tagging algorithm is applied to all MC files. For this the hit density in the SciFi is used; a target wall is considered to contain the interaction vertex if it accounts for at least 95% of the hits of the total SciFi hits. The first two target walls are excluded if the extended veto is applied. Furthermore the last target wall is omitted to ensure that the hadronic shower has sufficient space to develop and can be efficiently captured in the HCAL. The resulting distribution of reconstructed interaction walls is presented in Fig. 7, the remaining interaction walls constitute  $\approx 47\%$  of the overall statistics.

After applying all cuts, the muon DIS and PMB processes are fully suppressed. It should be reminded that the MC statistics of  $1 - 4e5$  for PMB and muon DIS are not sufficiently representative of the expected yields of  $\approx 10^6 - 10^8$  and the PMB and muon DIS processes are not fully suppressed in run data. The signal is reduced to  $\approx 3\%$  of the initial statistics and the NHB is reduced to  $\approx 0.8\%$ . It goes to show, that improving the discrimination between the  $\nu_\mu$ -CC DIS and NHB processes is very important for achieving a more efficient signal selection. To generally improve the extraction of the signal from the background processes, further analysis are performed in this work to find distinguishing parameters (see chapter 6). Possibly, these parameters could substitute the  $\nu_\mu$ -CC DIS selection cuts or be used in combination with a subset of cuts to select signal events and retain more statistics. For this and further analysis, only the pre-selection and fiducial cuts are applied due to the significant reduction of statistics for the PMB and muon DIS once the extended veto and selection cuts are applied. In this way, a sufficient amount of statistics is ensured, allowing for reliable analysis.

However, in the case of  $\nu_\mu$ -CC DIS and NHB, it has to be proven that the omission of the extended veto and selection cuts doesn't significantly change relevant distributions and introduce a bias into the results when comparing with the full applied cuts. For this the ratios of the distributions before and after the extended veto and selection cuts are calculated. If the resulting ratios are found to be approximately flat, then the shape of the distribution is preserved, justifying the use of the reduced cut set. An example of such cut ratio distributions is found in Fig. 8 for the hadron shower position in the US in Y, called y-barycenter  $y_B$  (details in chapter 3.4), for signal (blue) and NHB (red). Some fluctuations can be found in these ratios of up to  $\approx 0.1$ , nevertheless the ratios remain largely flat over the parameter range. Given the statistical limitations, this variation is deemed acceptable and the ratios sufficient to justify using the reduced cut set for all further analysis.

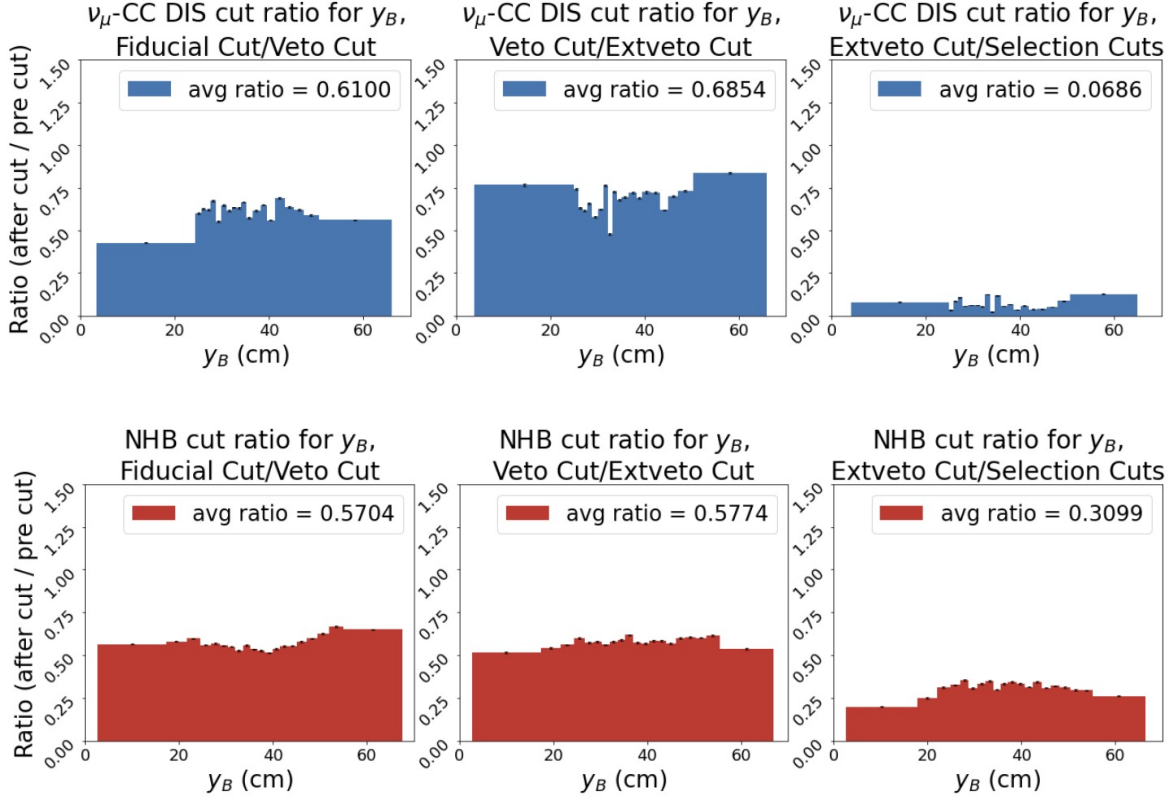


**Figure 8:** Ratios of the x-barycenter distributions before and after veto, extended veto and selection cuts for the signal (top) and NHB (bottom). A constant cut ratio indicates that the shape of the  $y_B$  distributions aren't affected by the implemented cuts.

### 3.4 Shower Reconstruction

The hadronic shower of the  $\nu_\mu$ -CC DIS interaction is reconstructed in the HCAL of SND, primarily in the US planes. Per plane the hadron shower position, called the barycenter  $x_B/y_B$ , and the hadron shower width  $\lambda_{x/y}$  in X and Y are defined and obtained. Additionally, the kinematics of the hadronic shower can be used to calculate the polar angle  $\theta$  and azimuthal angle  $\phi$ . This shower reconstruction algorithm is also applied to the background samples and all distributions are compared to identify distinguishing parameters between signal and background.

A schematic overview for the definitions of the barycenter and width of the hadronic shower in X and Y per event and US plane is given in Fig. 9. To begin with, the fired bars per event and plane are identified, as these are relevant for all following definitions. In the simulation we define a scintillator bar to "fire" if an energy deposition threshold of 2MeV is exceeded. Additionally, only a subset of bars is considered, so that 95% of the energy deposition of the plane is taken into account. This is done by starting with the bar with

the highest energy deposition of that plane and iteratively adding bars in decreasing order of energy until the threshold is reached.

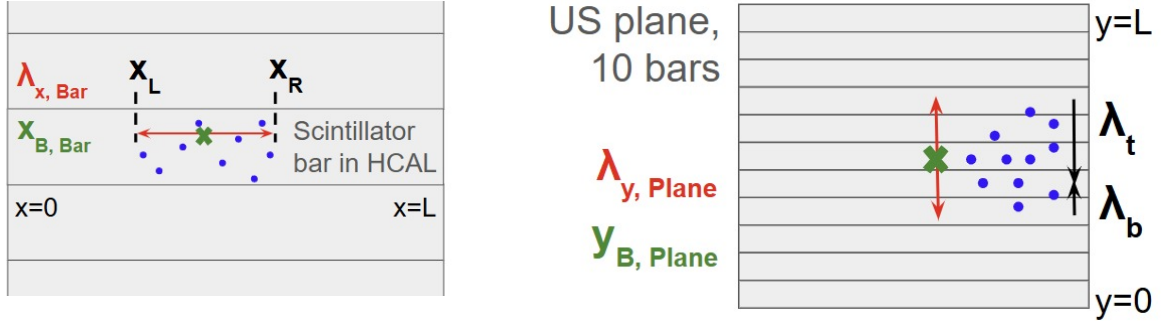


**Figure 9:** Definitions of the shower barycenters  $x_B/y_B$  and width  $\lambda_{x/y}$  in X (left) and Y (right) per US plane and event.

The definition of the barycenter  $x_B$  in X per US plane is as follows:

$$x_B = \sum_{\text{Fired Bars}} x_{B,\text{Bar}} \cdot \frac{E_{\text{loss,Bar}}}{E_{\text{loss,Plane}}}, \quad (5a)$$

$$x_{B,\text{Bar}} = \frac{(t_R + t_L)}{2} \cdot \bar{c}_{\text{scint,Bar}}, \quad (5b)$$

$$t_{R/L} = \frac{x_{R/L}}{\bar{c}_{\text{scint,Right/Left}}}. \quad (5c)$$

Where the barycenter is first calculated per fired bar  $x_{B,\text{Bar}}$  using the left most and right most MC points ( $x_L$  and  $x_R$ ) of that bar. These positions are converted to their respective time of flights,  $t_L$  and  $t_R$ , representing the travel time of the photons from  $x_L$  and  $x_R$  to the left and right side of the bar respectively. The average scintillator readout speed  $\bar{c}_{\text{scint,Bar}}$  per bar and per bar side  $\bar{c}_{\text{scint,Right/Left}}$  is used for this and obtained from detector measurements [10]. This mimics the behavior of the earliest photons arriving at the SiPMs on both bar sides and triggering data acquisition. Subsequently,  $x_{B,\text{Bar}}$  is weighted by the relative energy deposition  $\frac{E_{\text{loss,Bar}}}{E_{\text{loss,Plane}}}$  of that bar, the sum over all fired bars gives  $x_B$  for that plane and event.

The shower width  $\lambda_x$  in X is defined similarly:

$$\lambda_{X,Plane} = \sum_{\text{Fired Bars}} \lambda_{X,Bar} \cdot \frac{E_{loss,Bar}}{E_{loss,Plane}}, \quad (6a)$$

$$\lambda_{X,Bar} = (t_R - t_L) \cdot \bar{c}_{\text{scint},Bar}, \quad (6b)$$

here the difference of the travel times,  $t_L$  and  $t_R$ , is taken into account. In Y the barycenter is again first calculated iteratively per bar and weighted with the relative energy deposition of that bar:

$$y_{B,Plane} = \sum_{\text{Fired Bars}} y_{B,Bar} \cdot \frac{E_{loss,Bar}}{E_{loss,Plane}}, \quad (7a)$$

$$y_{B,Bar} = y_{Bar}. \quad (7b)$$

Per bar the barycenter  $y_{B,Bar}$  is simply defined as the position of the middle of that bar  $y_{Bar}$ . Finally, the shower width in Y takes the difference in the Y position between the highest most and lowest most fired bar,  $y_{Bar,max}$  and  $y_{Bar,min}$ :

$$\lambda_{Y,Plane} = y_{Bar,max} - y_{Bar,min}. \quad (8)$$

Alternative methods of defining the barycenters and widths of the shower are tested, the definitions described above are chosen for several reasons. For instance, a comparability between all X and Y distributions in both shape and value are expected, while tolerating some variation due to geometrical effects such as a gradient in the muon flux. Furthermore, the definitions shouldn't heavily be influenced by the normalization or energy deposition threshold chosen. Finally, when possible, comparisons to MC truth-level information is made and demonstrates good agreement.

In Fig. 10 the resulting barycenter distributions in X and Y are depicted (top row) as well as the corresponding residuals (bottom row). The residuals here represent the difference between the mean position per event and plane given from MC truth-level information and the corresponding barycenter. The narrow distribution of residuals in Y indicates a good agreement. In contrast, the broader distribution in X can be traced back to smearing applied in both the X position and the energy deposition in the MC files to simulate detector behavior. This behavior is expected in the detector due to electric noise, cross-talk and other

instrumental factors; given this the definition for X is considered acceptable. Column structures can be observed in the Y barycenter distribution and are attributed to the scintillator bar positions in Y, effectively smeared by the relative energy deposition as in eq. 7.

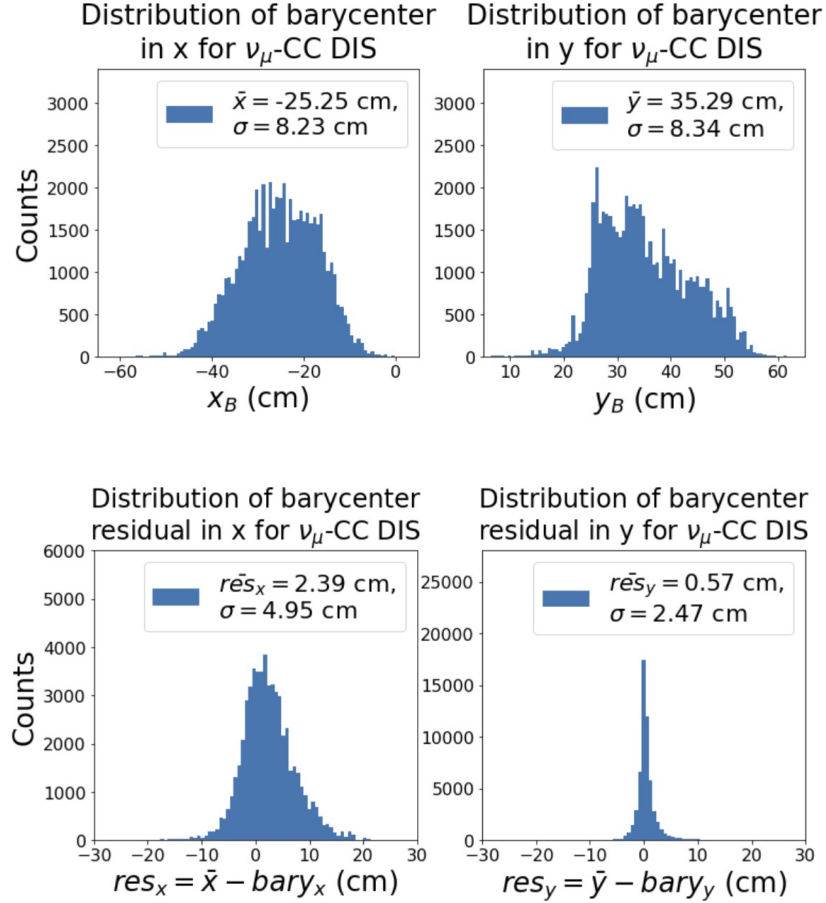


**Figure 10:** Top: Distributions of barycenters calculated in the US of the HCAL in X (left) and Y (right) per event and US plane. Bottom: Corresponding residuals, obtained using the MC truth-level position in X and Y per plane and event.

In Fig. 11 and 12 the  $\lambda_X$  and  $\lambda_Y$  distributions for all processes and per US plane are depicted. Negative  $\lambda_X$  values up to  $-5\text{cm}$  can be observed for all processes due to the smearing applied to the X-position and energy deposition; the  $\lambda_Y$  definition is not affected by the smearing. This behavior is also observed in the experimental data, more on this in chapter 5. Additionally, a common observation is the narrowing of all distributions in both  $\lambda_X$  and  $\lambda_Y$  with increasing US plane. Most interactions occur in the target system because of the larger mass and density compared to the HCAL. This explains the dying off hadronic

and electromagnetic (EM) showers in the US planes and the resulting diminishing tails. A further similarity between the different processes can be found in the dominating peak at around 0cm – 1cm. While this is more prominent in the background processes, it can still be found in the signal distributions, especially for the later US planes. These lambda values correspond to events and planes in which only one particle or a small, concentrated scattering of particles is detected. For example, in the case of the signal, the hadronic shower dies off and leaves the high-energy characteristic muon as the only signature. Similar residual muons or high-energy particles are found in the background processes, more prominent due to the smaller size of the hadronic and EM showers produced.

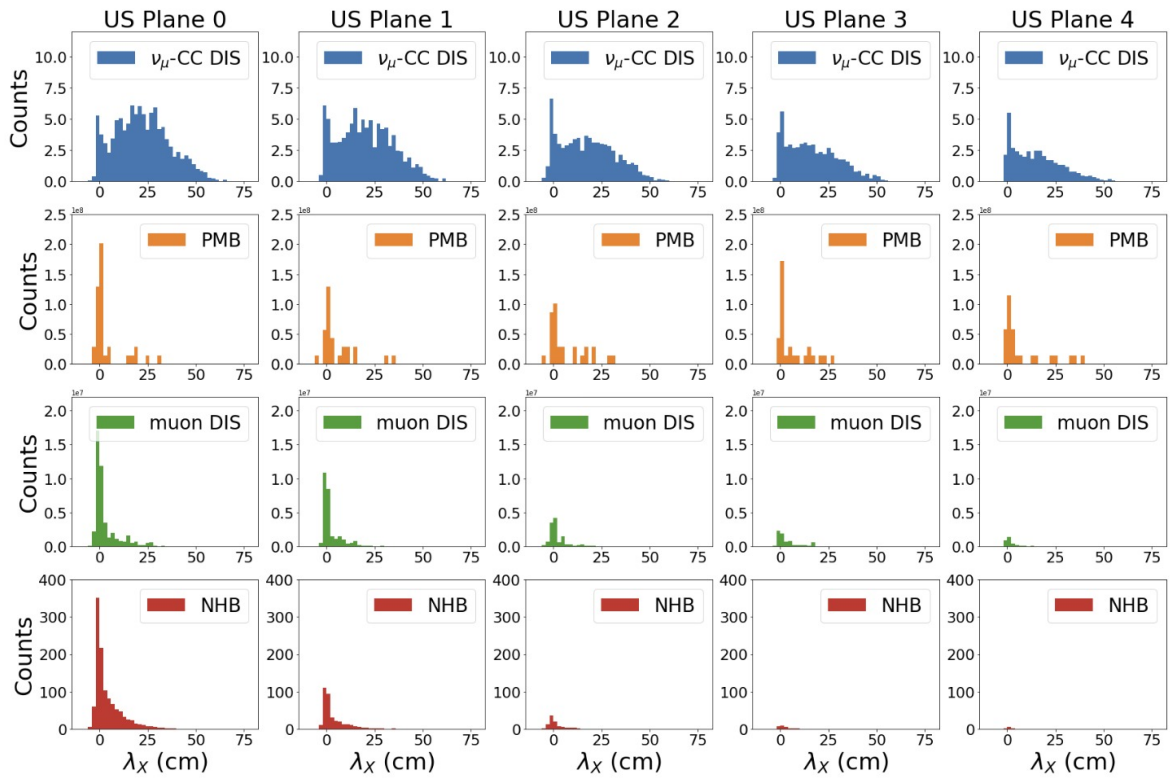


**Figure 11:** Distributions of  $\lambda_X$  per US plane for the signal (first row), PMB (second row), muon DIS (third row) and NHB (fourth row). The distributions are normalized to  $L = 36.8\text{fb}^{-1}$ .

As mentioned before, a symmetry in X and Y is expected of the shower width. A comparability can be found in the distributions for  $\lambda_X$  and  $\lambda_Y$  for certain important features: signal  $\lambda$  distribution spread over entire detector region, dying off shower width with increasing US plane and the 0cm peak for all processes. Only the distribution shape differs significantly.

As in the barycenter distribution for  $Y$  (Fig. 10), column structures corresponding to the ten scintillator bars per US plane are visible. For the background processes, the distributions are broader, possibly due to the differing methods because  $\lambda_Y$  doesn't use the relative energy of the bars or because of leakage in  $Y$ . Overall, the shower width in  $Y$  shows comparable behavior to  $X$  for both signal and background processes, confirming the chosen method and required symmetry.

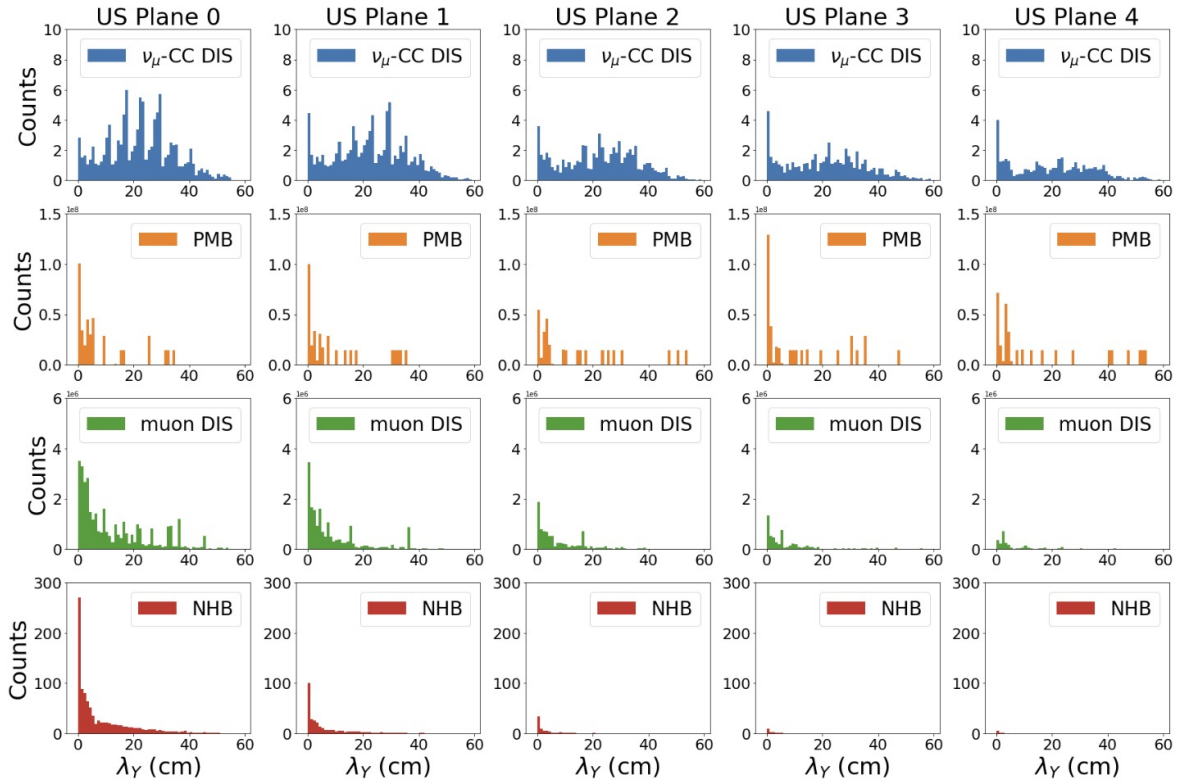


**Figure 12:** From top to bottom: signal, PMB, muon DIS and NHB distributions for  $\lambda_Y$  per US plane, normalized to  $L = 36.8\text{fb}^{-1}$ . The column structures, most prominent in the signal distributions, are traced back to the 10 scintillator bars per US plane.

However, significant differences are found between the  $\nu_\mu$ -CC DIS  $\lambda$  distributions and the background distributions. The former spanning over the entire detector range of 80 cm in  $X$  and 60 cm in  $Y$  owing to the characteristic hadron shower. Contrarily, the background processes are largely contained to  $\lambda_X$  and  $\lambda_Y < 40\text{cm}$ . In singular cases, the  $\lambda$  methods are still sensitive to outlying high-energy muons or scatterings of particles occurring in addition to a hadronic or EM shower and resulting in large lambda values. An overview of average  $\lambda$  values per plane is shown in Fig. 13.

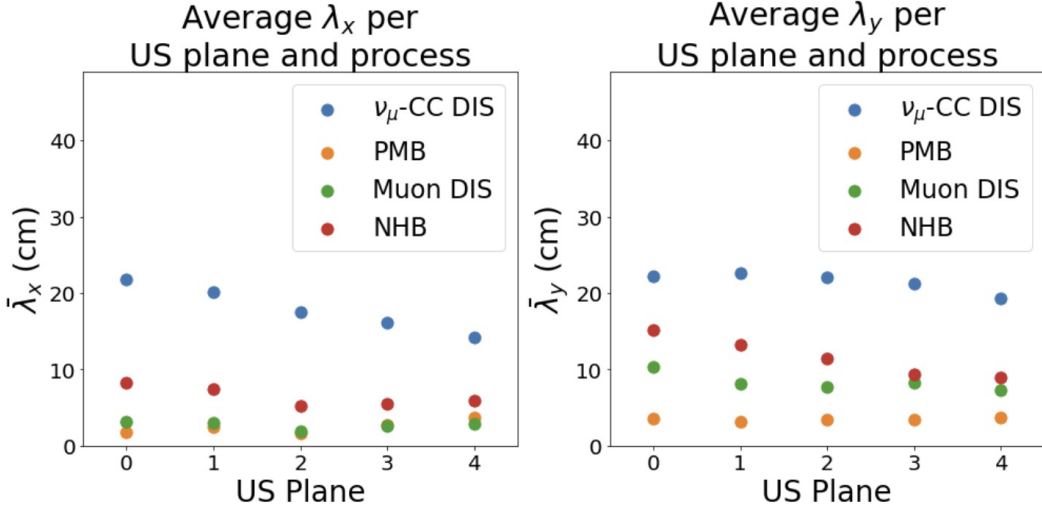


**Figure 13:** Average  $\lambda_X$  and  $\lambda_Y$  per US plane and process. The average shower width for both X and Y for the signal is between 7cm and 13cm greater than that of the background processes.

The discrepancy found between signal and background in the distributions, as well as the attenuation of the  $\lambda$  tails with increasing US plane, are clearly reflected here. Notably, the quantitative difference between the different processes and characteristics for each is brought to the forefront. For the signal,  $\lambda_X$  is about 7 – 13cm larger than for the next leading background process, NHB, while  $\lambda_Y$  is 7 – 12cm larger. The difference in  $\lambda$  to the PMB and muon DIS ranges from 13 – 20cm. With this, a significant parameter has been found to help discriminate between signal and background and will be taken advantage of in chapter 4.2.

Furthermore, the lambda distributions can be analyzed depending on where the interaction originates, such plots are found in Fig. 14 for  $\lambda_X$  and  $\lambda_Y$ . For  $\lambda_X$  the linear decline is found for each interaction wall to a varying degree. The attenuation of  $\lambda_X$  is stronger for earlier interaction walls, leading to larger average values for the later interaction walls. However,  $\lambda_Y$  shows no such underlying longitudinal dependency. It is likely, that this differing dependency is due to the methods of calculating  $\lambda_X$  and  $\lambda_Y$ . The latter relies on the granularity of the horizontal scintillator bars in the US, whereas  $\lambda_X$  has no such restriction on the resolution. It follows, that  $\lambda_X$  is more sensitive to fluctuations and also underlying effects such as the attenuation of the hadronic shower. It is clear, that a possibility of increasing the discriminating power of the shower width lies in the interaction wall dependency of  $\lambda_X$ . Only selecting the later interaction walls, as is done when applying the extended veto and selection cuts, results in a larger average  $\bar{\lambda}_X$  value. A lack of statistics prohibits the application of the selection cuts, merely leaving this as a suggestion for future analysis.

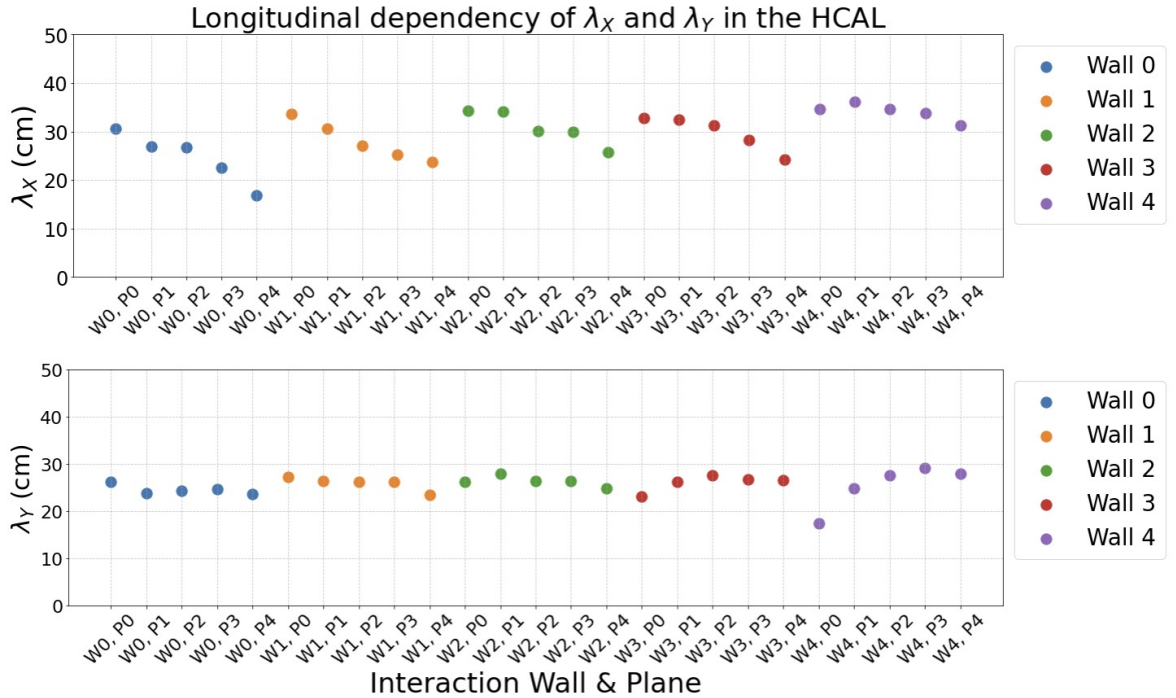


**Figure 14:** Depicted are the average  $\lambda_X$  (top) and  $\lambda_Y$  (bottom) values per interaction wall and US plane for  $\nu_\mu$ -CC DIS interactions. The attenuation of the hadron shower through the HCAL is reflected  $\lambda_X$  but not in  $\lambda_Y$ , likely due to the asymmetry of the US in X and Y.

Additionally, the definition of  $\lambda_X$  and  $\lambda_Y$  is adjusted and extended to the SciFi and DS. For the definition in the SciFi a subset of channels is utilized. Firstly, the channel with the highest energy deposition is identified, further channels are iteratively added to the set in order of descending energy deposition until 95% of the total SciFi energy deposition of that event is accounted for. The definitions of the shower width in the SciFi are then:

$$\lambda_{X,\text{SciFi}} = x_{\max} - x_{\min}, \quad (9a)$$

$$\lambda_{Y,\text{SciFi}} = y_{\max} - y_{\min}, \quad (9b)$$

where  $x_{\max}$ ,  $y_{\max}$  and  $x_{\min}$ ,  $y_{\min}$  are the position of the channels with maximum and minimum X-/Y-coordinate.

In the DS of the HCAL, the procedure of obtaining  $\lambda_{X,\text{DS}}$  and  $\lambda_{Y,\text{DS}}$  is the same as for the SciFi, differing only in the use of scintillator bars instead of SiPM channels. These definitions were chosen for their comparability with the shower width definition in the US of the HCAL and due to the increased granularity of the SciFi and DS. The resulting distributions are

presented in Fig. 15. Similarly to the  $\lambda$  distributions in the US, the signal is spread over the entire parameter range. Contrarily, the background processes are present over the entire parameter range but tend to smaller  $\lambda$  values. This is reflected in the average  $\lambda_X$  and  $\lambda_Y$  values for the signal compared to the background:  $\bar{\lambda}_{X/Y,\text{SciFi}}$  is  $\approx 8\text{cm}$  and  $\bar{\lambda}_{X/Y,\text{DS}}$  is  $\approx 3\text{cm}$  larger than the next leading background process (NHB). Through this, the definition of  $\lambda_{X/Y}$  in the SciFi and DS proves to be a valuable addition to the analysis of the hadron shower width and is taken advantage of in later analysis (see chapter 4.2).

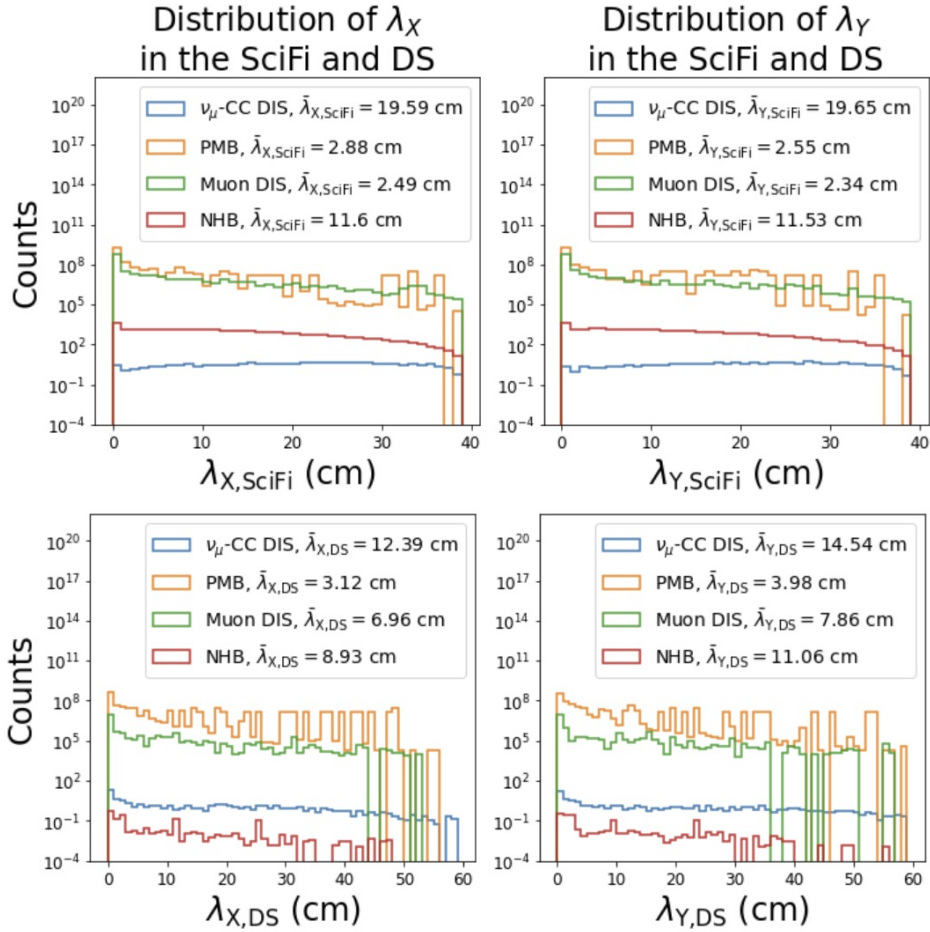


**Figure 15:** The  $\lambda_X$  and  $\lambda_Y$  definitions are extended to the SciFi (top) and DS of the HCAL (bottom) to obtain the depicted distributions. As before, the average  $\lambda_{X/Y}$  values of the signal are  $\approx 3 - 8\text{cm}$  larger than the next leading background process (NHB).

Finally, as mentioned before, the polar and azimuthal angles  $\theta$  and  $\phi$  can be calculated for the hadron showers in the HCAL. For this a minimum of three fired US and DS planes is required, from which the X- and Y-barycenters can be calculated. Through these a linear fit can be applied and the slope and angles are obtained as follows:

$$\text{slope}_X = \frac{dx}{dz} \text{ and } \text{slope}_Y = \frac{dy}{dz}, \quad (10a)$$

$$\theta = \arccos \left( \frac{1}{\sqrt{1 + \text{slope}_X^2 + \text{slope}_Y^2}} \right), \quad (10b)$$

$$\theta_X = \arctan(\text{slope}_X) \text{ and } \theta_Y = \arctan(\text{slope}_Y), \quad (10c)$$

$$\phi = \arctan \left( \frac{\text{slope}_Y}{\text{slope}_X} \right). \quad (10d)$$

Corresponding distributions are found in Fig. 16. It is apparent, that the azimuthal angle  $\phi$  is broadly distributed across the full parameter range for all process. This more or less uniform distribution is expected as there is no preferred direction for the hadron shower production or the other processes. Nevertheless, regions with pronounced peaks are observed, possibly coinciding with hot-spots in the muon and neutrino flux. Restrictions on the position and dimension of SND@LHC in the TI18 tunnel mean these hot-spots are more or less fixed in their position for a given detector configuration. Consequently, the peaks are not deemed significant for the purpose of this analysis and not investigated further.

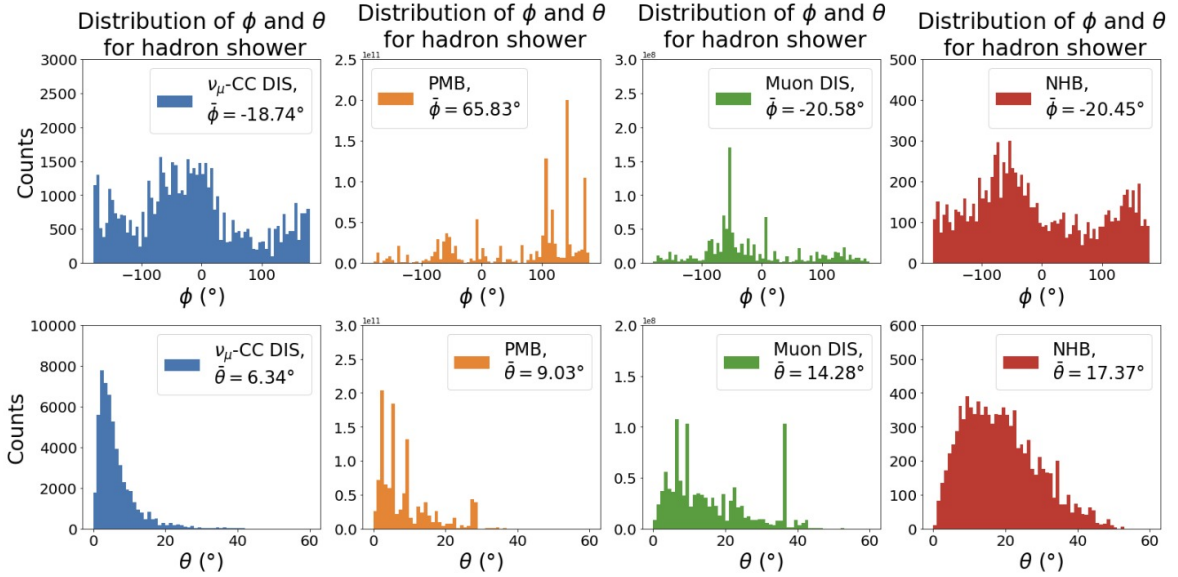


**Figure 16:** Distribution of the azimuthal angle  $\phi$  (top) and the polar angle  $\theta$  (bottom) for the hadron shower in the HCAL for all processes.

For the polar angle  $\theta$ , the observed distributions behave roughly as expected for the

corresponding processes. The  $\nu_\mu$ -CC DIS distribution is largely contained to  $\theta < 20^\circ$ , the PMB and muon DIS to  $\theta < 30^\circ$  and the NHB ranges up to  $\approx 50^\circ$ . Larger angles in the PMB are primarily caused by secondary EM-showers. Overall, the varying parameter regions for the signal and background processes indicate that the polar angle could be used as a discriminant for further analysis.

In summary, in this chapter definitions are found for the hadronic shower position  $x_B/y_B$  and width  $\lambda_{X/Y}$  in the US of the HCAL and analyzed for all relevant processes. Both in X and Y the signal shows an average hadronic shower width of 7 – 13cm larger than the background processes, proving to be a possible discriminator. Additionally, the definition of the shower width is extended to the SciFi and the remainder of the HCAL. Here the  $\lambda$  distributions in the DS prove to further enhance the discriminating power of this parameter due to the average  $\bar{\lambda}$  values of the signal being  $\approx 2 - 6$ cm larger than the background. Finally, the hadronic shower position in the HCAL is taken advantage of by applying a linear fit through these and using the fit slope to extract the polar angle  $\theta$  and azimuthal angle  $\phi$ . The former shows distributions for the signal ranging up to  $\theta \approx 20^\circ$ , whereas for the background the distributions range up to  $30 - 50^\circ$ . Together with the shower width, several significant parameters have been found to distinguish between signal and background and will be employed for this purpose in further analysis in later chapters.

### 3.5 Muon Reconstruction

In this chapter the reconstruction procedure of the outgoing muon characteristic for  $\nu_\mu$ -CC DIS interactions is introduced. For this a clustering algorithm is applied to the hits found in the DS of the HCAL per event. Subsequently, a fitting algorithm is applied and some requirements are enforced to select the resulting muon track candidate. As with the hadron shower, the kinematics of the muon can be taken advantage of to obtain the polar and azimuthal angles. All methods are applied to the signal as well as all background processes and compared.

Firstly, the clustering algorithm applied to hits in the DS planes of the HCAL searches for neighboring fired bars. The algorithm iterates through all hits and identifies a cluster as two fired bars that are either adjacent or next-to-adjacent in horizontal or vertical projections. All such clusters are found per event and fed into the track fitting algorithm, Genfit (Generic Track-Fitting Toolkit) [11]. In this toolkit, the fired bars in the clusters are modeled as wire measurements, where the bars are abstracted as a line in space. The fitting is performed using

a Kalman filter, which initializes a seed state and subsequently finds the position of closest approach (POCA) between the lines and predicted track. The track state and covariance are updated by iteratively calculating the residuals and minimizing these to find the best fit parameters through convergence. The spatial resolution of 0.3cm for the DS bars is passed as an initial estimate for the covariance matrix to the fit. Internal requirements of this fitting method are: three DS planes must be hit and each plane must contain at most five clusters. Finally, several tracks are produced and the one with the lowest  $\chi^2$  is chosen as the final muon track candidate for that event. A Runge-Kuttar track representation for  $\mu^-$  is chosen and the detector geometry is set to extrapolate the track to the interaction vertex identified in the target system. This representation contains a FitStatus, which carries information about the quality of fit and convergence. Additionally, a FittedState object gives all relevant track parameters such as identified clusters, track direction and momentum,  $\chi^2$  and numbers of degrees of freedom (dof).

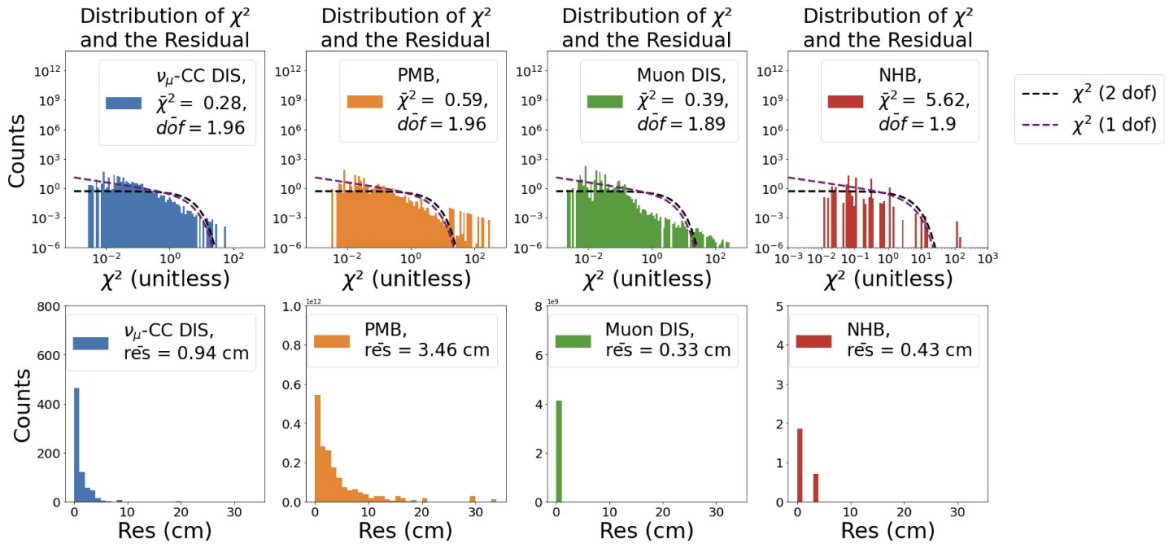


**Figure 17:** Distributions for the  $\chi$  (top) and the residuals (bottom, see eq. 11a) for the signal and background processes. The expected  $\chi^2$  fits for 1 or 2 dof are also plotted.

In this way, muon track candidates are found and evaluated using the  $\chi^2$  distributions found in Fig. 17 (top). The  $\chi^2$  fits for one and two dof are added, as these correspond the number of dof yielded by the Genfit algorithm throughout the events. The expectation value of a  $\chi^2$  distribution equals the dof, which serves a reference for evaluating the quality of the track fits. In the case of the  $\nu_\mu$ -CC DIS and PMB the average dof is  $\approx 1.96$ , whereas the

average  $\chi^2$  value is  $\bar{\chi}_{\nu_\mu}^2 = 0.28$  and  $\bar{\chi}_{\text{PMB}}^2 = 0.59$  respectively. For the muon DIS one observes  $\approx 1.89$  dof and  $\bar{\chi}_{\text{muonDIS}}^2 = 0.39$ . For all these processes the average  $\chi^2$  comes in at roughly 1.5 below the expected value. Additionally, small residuals are found for the signal and muon DIS in Fig. 17 (bottom plots). The residuals between the reconstructed muon track  $\text{tr}_{\text{recon}}$  and the MC truth level muon track  $\text{tr}_{\text{MC}}$  are calculated as follows:

$$\text{Res} = \sqrt{dX^2 + dY^2}, \quad (11a)$$

$$dX = \text{tr}_{\text{MC},X} - \text{tr}_{\text{recon},X}, \quad (11b)$$

$$dY = \text{tr}_{\text{MC},Y} - \text{tr}_{\text{recon},Y}. \quad (11c)$$

This suggests, that the fit performs well for these processes, but that the errors may be overestimated. Seeing as the resolution of the DS detector planes are input as the initial guess of the covariance matrix, it may be that the resolution is being underestimated and leading to the discrepancy found in the  $\chi^2$  distributions. For example, it has been observed that the outgoing characteristic muon of these processes can hit more than one scintillator bar in the DS per plane and projection. It follows, that in future analysis the resolution could be adjusted to account for this effect. The overall acceptable performance of the muon reconstruction algorithm for the signal and muon DIS is due to these interactions being forced in the target system and rock upstream of the detector respectively. This allows enough time for the corresponding hadronic and EM showers to die off and leave a clear outgoing muon signal that is easily reconstructible by the tracking algorithm.

In the case of the PMB, the residuals have a larger spread than the signal and muon DIS processes. Several parameters, such as the longitudinal momentum  $p_z$  of the incoming muon, energy loss of events in the DS and the hit count per event in the DS, are considered and compared between the PMB and muon DIS processes. The goal is to find a possible explanation for the poorer fit quality of PMB events; the relevant parameters can be seen in Fig. 18. The left most diagram shows comparable distributions between the PMB and muon DIS for the longitudinal momentum of the incoming muon, the average values overall all MC events are  $p_{z,\text{PMB}} = 827.7 \text{ GeV}$  and  $p_{z,\text{muonDIS}} = 751.3 \text{ GeV}$ . It follows, that the momentum of the PMB is slightly larger than that of the muon DIS, but are overall in the same parameter range. Looking at the energy loss and hit count per event in the DS - Fig. 18 middle and right respectively - shows higher average values of  $E_{\text{loss}} = 0.0292 \text{ GeV}$  and 9 hits for the PMB compared to  $E_{\text{loss}} = 0.006 \text{ GeV}$  and 1 hit for the muon DIS. This shows a

much larger activity and energy deposition of the passing muon events in the DS. The muon DIS MC files are forced to interact in the cavern upstream of the detector, an attenuation of muon DIS activity by the DS is expected. Additionally, the large activity found of the PMB in the DS is due to processes included in these files such as: Bremsstrahlung, lepton pair production and delta ray emission. These processes are excluded in the muon DIS files, even though the incoming and outgoing muon of the respective DIS interaction are comparable to the muons of the PMB MC file. It follows, that the different processes included in the PMB compared to the muon DIS, causing the discrepancies in activity and energy deposition in the DS, lead to a poorer identification of clusters and thus a poorer performance of the fit and tracking algorithm.

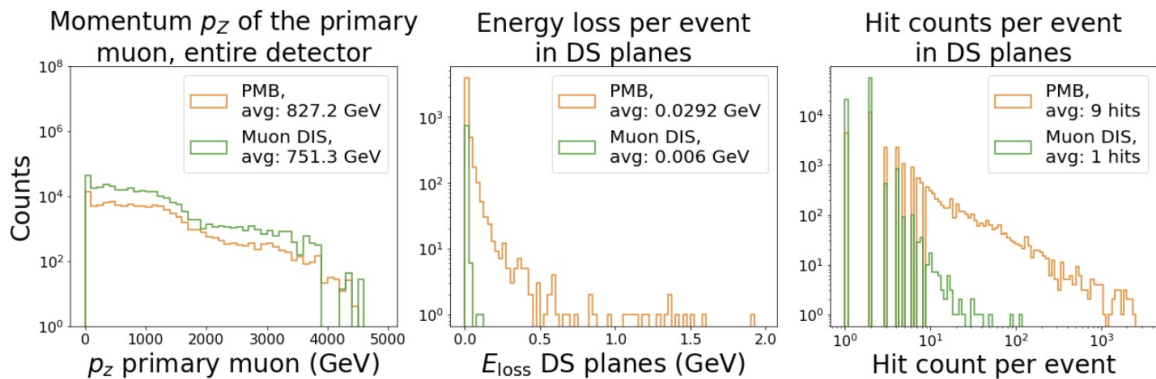


**Figure 18:** The left plot depicts the comparable longitudinal momentum  $p_Z$  of the primary muon for PMB and muon DIS. The hit count per event (middle) and DS plane (right) varies between the PMB and muon DIS processes. An average hit count of up to 12 hits is reached for PMB events, whereas on average only two hits are recorded per muon DIS event in the DS.

Finally, the average  $\chi^2$  value for the NHB is  $\bar{\chi}^2 = 5.62$  with an expectation value of  $\approx 1.9$ . This reflects an expected poor performance of the tracking algorithm for NHB due to the lack of outgoing muons to reconstruct, also explaining the comparatively low statistics found in Fig. 17 for NHB.

In summary, the tracking algorithm performs as expected for the different processes. Reliable fits are produced for the signal and muon DIS processes and the poor fits of NHB are expected due to the lack of outgoing muons for this process. A possible explanation for the poorer fit quality for PMB events is found. The fits are still deemed acceptable in the

context of this work but should be improved for future studies. Additionally, the resolution could be adjusted for the possibility of muons hitting more than one scintillator bars in the DS.

The X-&Y-position of the reconstructed muon tracks in the DS is depicted in Fig. 19. Here the red box represents the DS fiducial area as described in chapter 3.3. For the most part the tracks are contained within the fiducial area, indicating an accurate representation of the outgoing muons. The lack of statistics in the case of NHB is due to the lack of a reproducible outgoing muon for this process, as confirmed in the efficiency of selection cut 11 of Table 2.

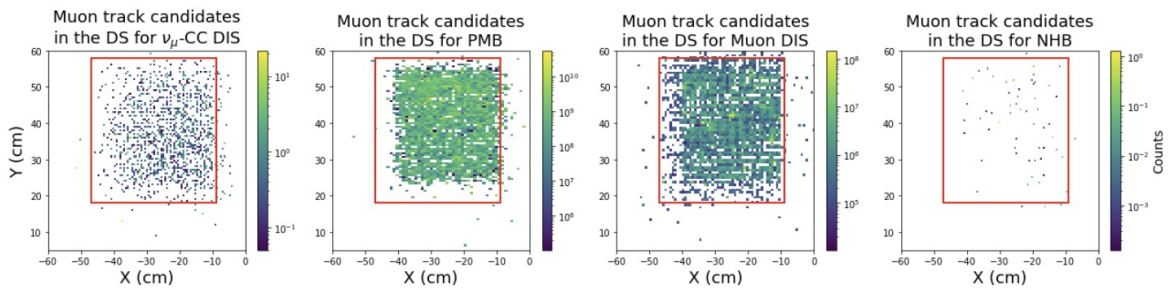


**Figure 19:** Position of the reconstructed muon track candidates in the DS of the HCAL, mostly confined in the DS fiducial volume (highlighted in red).

As with the hadron shower, it is possible to gain information about the azimuthal angle  $\phi$  and the polar angle  $\theta$  from the reconstructed muon tracks. For this, the directional vectors of the tracks are extracted and the angles are calculated as in eq. 10a - 10c and the corresponding distributions can be found in Fig. 20. As in the azimuthal angle distributions for the hadronic shower,  $\phi$  is spread out over the entire parameter range. Here, distinct structures are found in the same positions for each process. The size, symmetry and position of the structures induces the hypothesis, that these reflect the scintillator bars in the DS, vital for the muon track reconstruction and the subsequent angle calculation. A further investigation into these structures is not performed in the scope of this work and not deemed influential on the remainder of the analysis.

As before, the behavior of the polar angle distributions of the different processes is comparable to that of the hadronic shower (Fig. 16). The signal distribution is primarily contained within angles up to  $\approx 8^\circ$ , the PMB extends to  $\approx 12^\circ$ , the muon DIS up to  $\approx 3^\circ$  and the NHB up to  $\approx 40^\circ$ . Notable is the lack of statistics for NHB due to the lack of obtained muon track

candidates. Due to the nature of NHB events and the scattering of neutral hadrons over the entire detector range, the polar angles obtained from the reconstructed muon track are also scattered over a large parameter range. This behavior is in accordance with expectations and can be summarized, together with the poor fit quality (Fig. 17), as an artifact of applying the tracking algorithm to NHB events which lack a trackable outgoing muon. The  $\theta$  signal distribution peaked at  $0^\circ$  with a longer tail up to  $40^\circ$  is also expected due to the hadronic shower. The peak is again explained through the attenuation of the shower in later US and DS planes, resulting in smaller polar angles. As before, the muon DIS interaction originating upstream of the detector and the following attenuation early in the detector explains the narrow  $\theta$  distribution observed due to smaller energy depositions in the detector components. Contrarily, the larger energy deposition of the PMB (see Fig. 18, middle) gives rise to the broader  $\theta$  distribution when compared to the muon DIS. In general all four processes show different behavior, where signal and PMB are most similar in size and shape, and the polar angle of the reconstructed muon track is identified as an additional parameter to discriminate between signal and background processes.

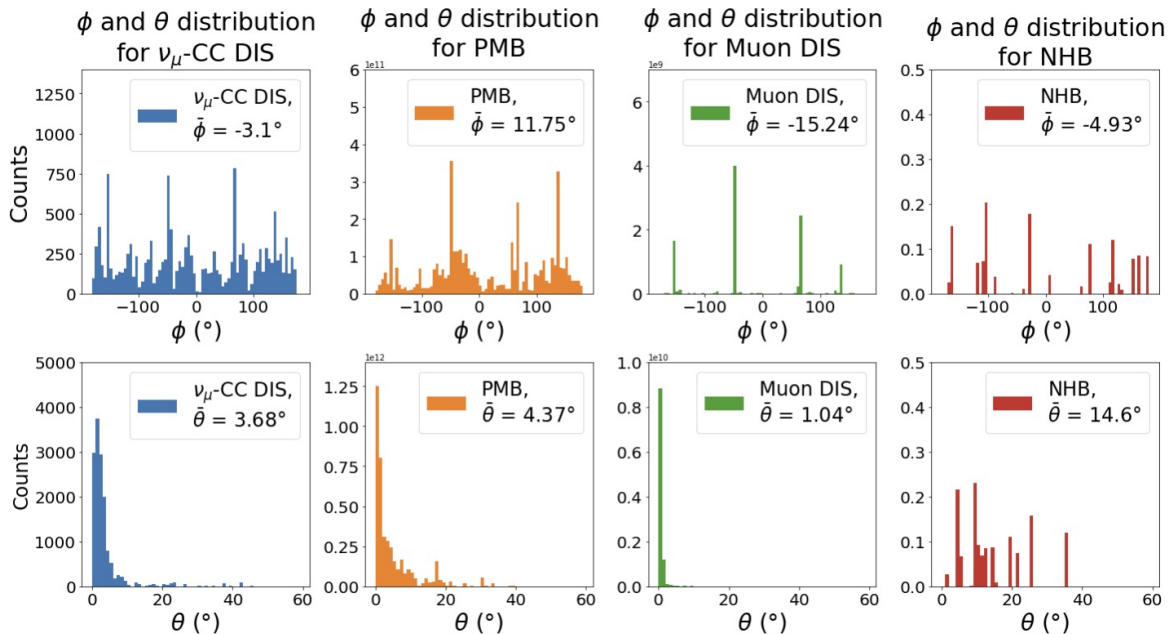


**Figure 20:** Azimuthal angle  $\phi$  (top) and polar angle (bottom) distributions for all processes.

A lack of reconstructible muon track candidates accounts for the low statistics of NHB.

Together with the obtained hadron shower width and position (chapter 3.4), the reconstructed muon track candidates can be used to display events in the HCAL of the detector as

is done in Fig. 21. The left image displays the hadron shower and muon in a 2d-projection of the first US plane and the right image depicts the reconstructed muon track candidate and hadron shower barycenters throughout the HCAL. In this way the signal and its components have successfully been defined and reproduced in the HCAL of the detector and the presented methods applied to all background processes.

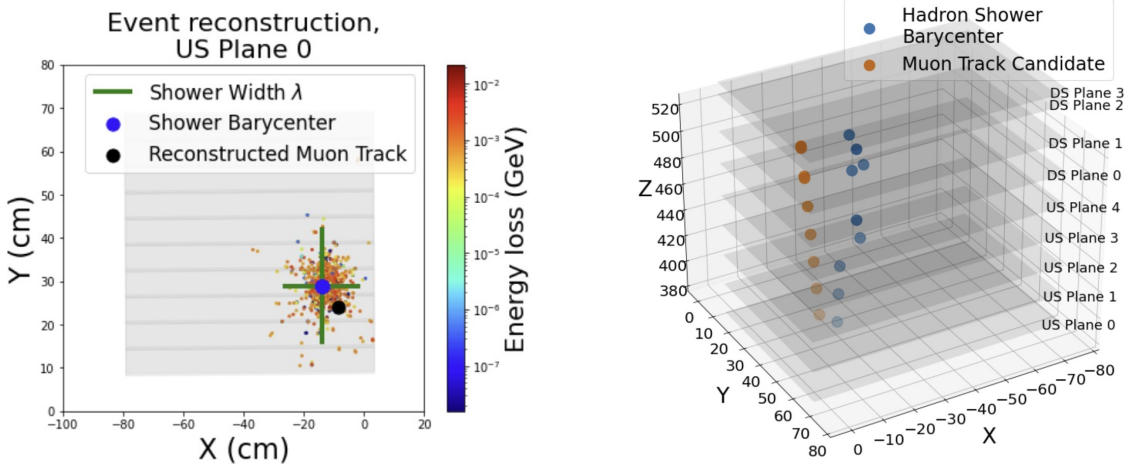


**Figure 21:** Reconstruction of an event using MC data in US plane 0 on the left, with corresponding scintillator bars in grey. The shower position (barycenter, blue), width  $\lambda$  (green) and reconstructed muon track candidate (black) as previously introduced are depicted. A 3d reconstruction of an event, featuring the hadron shower barycenters and reconstructed muon track, in the HCAL is seen on the right.

In conclusion, in this chapter a clustering algorithm is used together with the Genfit tracking algorithm to reproduce the characteristic muon of the  $\nu_\mu$ -CC DIS. The performance of these algorithms are tested for the signal and background processes. It is found to perform well for the signal, PMB and muon DIS processes, whereas for the NHB a lack of a characteristic muon for this process explains the poor fits and lack of statistics obtained. With the obtained fits, the azimuthal angle  $\phi$  and the polar angle  $\theta$  are extracted and compared. Here, the polar angle shows process dependent behavior, with the distributions extending to the following angles:  $\theta_{\nu_\mu} < 8^\circ$ ,  $\theta_{\text{PMB}} < 12^\circ$ ,  $\theta_{\text{muonDIS}} < 3^\circ$  and  $\theta_{\text{NHB}} < 40^\circ$ . These distinct parameter regions allow for the usage of the polar angle of the reconstructed muon track candidates as a further discriminator between signal and background.

### 3.6 Summary

In the following, the procedures of the previous chapter are summarized and discussed: the underlying configuration of SND on which this work is based, MC file production and normalization, applied selection cuts to extract  $\nu_\mu$ -CC DIS events from background events, the characterization of the hadron shower primarily in the US and finally the reconstruction of muon tracks from DS data.

The simulation constructed in this work is based on the configuration used in 2022, featuring a crossing angle of  $-160\mu\text{rad}$  and an integrated luminosity of  $L = 36.8 \text{ fb}^{-1}$ . The physics processes taken into consideration in this work and their expected yields in 2022 are:  $\nu_\mu$  charged-current deep inelastic scattering ( $157 \pm 37$ ), passing muons ( $5.0 \cdot 10^8$ ), muon deep inelastic scattering ( $1.65 \cdot 10^6$ ) and a neutral hadron background ( $8.61 \cdot 10^4$ ). The procedure of creating MC files using FLUKA, GEANT4, GENIE and PYTHIA as well as the normalization weights applied to these files to obtain the desired integrated luminosity of  $L = 36.8 \text{ fb}^{-1}$ , is described. Consequently, a series of selection cuts is applied to the MC files with the goal of eliminating all background events. These cuts include the pre-selection cuts, placing a requirement on the energy deposition to mimic detector behavior, the fiducial volume cuts, to remove events that can't be fully reconstructed within the detector volume, the extended veto cuts, to remove charged particles mostly originating from background processes and finally the  $\nu_\mu$ -CC DIS selection cuts, using detector features characteristic to signal events to filter for these. An observation made through the cut efficiencies of the veto cuts is that adding the first two SciFi stations doesn't significantly impact the signal-background ratio. It follows, that the addition of these cuts is superfluous and it can be considered to remove these in future analysis to retain larger statistics. Furthermore, comparing the remaining statistics before and after the selection cuts results in a decrease of: 24.07% to 0.03% for  $\nu_\mu$ -CC DIS, 0.06% to 0.00% for PMB, 0.45% to 0.00% for muon DIS and 12.002% to 0.008% for NHB. It goes to show, that a large discrepancy between signal and background is already present before the selection cuts. Ideally, some of the selection cuts could be dialed back in place of a set of highly discriminating parameters in combination with a well tuned analysis method as an alternative approach of obtaining pure signal samples with increased statistics.

An essential component of the simulation introduced in the previous chapter is the characterization of the hadron shower. For this definitions are put forth for the shower position  $x_B/y_B$ , called barycenter, in the HCAL and for the hadron shower width  $\lambda_{x/y}$  in the HCAL and SciFi. Comparing the  $\lambda$  distributions between the signal and background processes shows

discrepancies of 7–13cm for  $\lambda_X$  and  $\lambda_Y$ . Additionally, the polar angle  $\theta$  of the hadron shower is obtained by applying a linear fit through the barycenters in the HCAL and extracting the resulting slope. This parameter also shows varying behavior between signal and background distributions. With this, two parameters are found with decent discrimination power that can be taken advantage of in further analysis.

The second main component of the simulation is the characterization of the outgoing muon. This is done by applying a clustering and fitting algorithm to DS data to get reconstructed muon tracks. The performance of the tracking algorithm is examined by looking at the  $\chi^2$  distributions of the resulting tracks. Overall, the fit performs well. An exception lies in the fit performance for NHB, which is understood though and unavoidable due to the lack of an outgoing muon for this process. Furthermore, the PMB shows a broader distribution for the track residuals than the signal and muon DIS. Possibly, this has to do with a larger energy deposition and hit count of passing muon processes compared to muon DIS events. The procedure for creating the MC files for the PMB and muon DIS files also varies, possibly causing differing processes to occur and result in a poorer performance of the tracking algorithm. This is not yet fully understood and improvements must be made either in understanding the PMB and muon DIS MC files or in the tracking algorithm itself. Furthermore, it is advised to increase the estimation of the DS resolution, which is utilized in an initial estimation of the covariance matrix. Particles are able to leave hits in more than one DS scintillating bar at the same time, possibly explaining the low average  $\chi^2$  values for signal of 0.26, for PMB of 0.59 and for muon DIS of 0.39 compared to the expected value of  $\approx 2$  (track = dof). Nevertheless, the performance of the tracking algorithm is considered to be acceptable and is used for the remainder of this work. As before, the azimuthal angle  $\phi$  and polar angle  $\theta$  are extracted from the reconstructed muon tracks; the average polar angle is also identified as a parameter with discrimination power between signal and background.

In conclusion, the selection cuts used in previous works such as [2] was examined and possibly contains some redundancies or inefficiencies. Here lies a possibility of combining a subset of cuts and an effective analysis strategy, based on discriminating parameters mentioned above, to gain higher statistics with the same efficiency. For this, the set of parameters identified will be utilized as the basis for further analysis in chapter 4.

## 4 Classification Strategies

After identifying a set of parameters showing deviations in their value ranges for the signal and background processes, several analysis methods are applied attempting to extract the  $\nu_\mu$ -CC DIS. The first of these, presented in chapter 4.1, uses likelihood based approaches focusing on the discrimination power of individual parameters to define signal-like events or parameter regions. The hadron shower width  $\lambda$  plays a central role in these efforts. Subsequently, a boosted decision tree (BDT) is constructed and trained in chapter 4.2. For this purpose, the individually limited discrimination power of different parameters is combined to train the BDT to classify a set of events sampled from signal and background processes. The trained BDT can be applied to an unseen dataset and classify these events in the same way.

### 4.1 Likelihood-based Methods

In this chapter, two likelihood-based methods are introduced and evaluated. The first of these aims to classify individual events as signal-like or background-like based on calculated likelihood ratios (LR), using the probability mass function (PMF) of the respective lambda distribution. The second method uses the raw counts of the same lambda distributions to create a composite model of the signal and background processes that can be fit to run data. In this way, the relative contribution of signal and background processes in the observed data can be quantitatively measured.

#### 4.1.1 Likelihood Ratio Test

In the following, the definition and results of the likelihood ratio analysis is presented, based on the previously discussed hadron shower width  $\lambda$  (see chapter 3.4). The goal of this is to classify individual events as signal or background depending on their calculated LR and a determined cutoff value.

In a first step, the PMF is essential and obtained from the  $\lambda$  distributions for each process. An example is given in Fig. 22 (top row) for  $\lambda_X$ . From this the likelihood  $L(\text{Process})$  of observing a given set of  $\lambda_X$  values per event and US plane is acquired for the process under investigation. Likewise, the likelihood  $L(\text{BG})$  that this same set of  $\lambda_X$  values originates from the background (BG) - the adjunction of the PMB, muon DIS and NHB processes - is extracted. With  $L(\text{Process})$  and  $L(\text{BG})$  in hand, the LR per event and US plane is given for the process of interest as:

$$LR = \frac{L(\text{Process})}{L(\text{BG})}. \quad (12)$$

Seeing as the parameter ranges of  $\lambda_X$  vary between the different processes, a penalty term is applied for empty bins in the BG to avoid a division by zero. Additionally, this emphasizes the cases where the likelihood of a  $\lambda_X$  value originating from the process under investigation is non-zero, while the corresponding background likelihood is zero. The penalty term is set to a very small, arbitrary value of  $10^{-20}$  and was chosen for its sensitivity without going beyond the scope of the LR value range. When presenting the final LR distributions, the normalization weights need to be applied, as introduced in chapter 3.2.2. The LR distributions corresponding to  $\lambda_X$  can be found in Fig. 22 (bottom row).

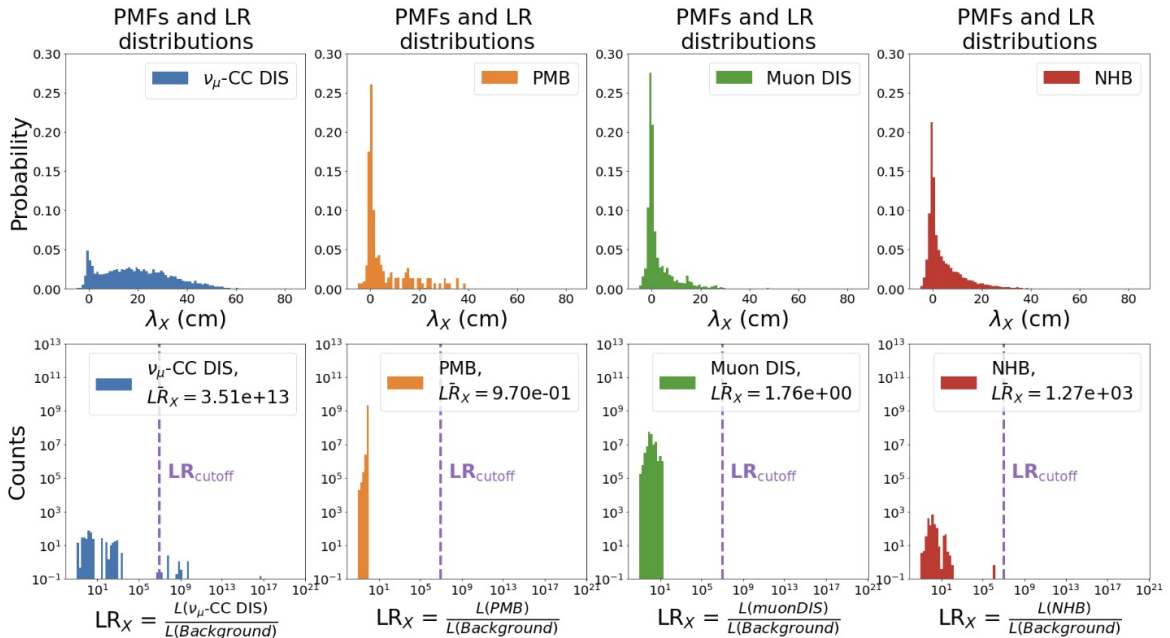


**Figure 22:** The top row depicts the PMFs for  $\lambda_X$  for the signal (blue) and the background processes. LR distributions are found in the bottom row with a cutoff value of  $LR_{\text{cutoff}} = 10^7$  determining if an event is signal- or background-like.

For all LR distributions there is a large peak in the  $10^{-1} - 10^3$  range, this can roughly be associated with  $\lambda_X < 40\text{cm}$  values. All processes contain values in this parameter range, leading to large  $L(\text{BG})$  and subsequently small LR values. Besides these peaks, the  $\nu_\mu$ -CC DIS and NHB also possess LR values larger than  $10^3$ , associated with  $\lambda_X > 40\text{cm}$  values. This approach allows for the identification of a signal-enhanced region within the LR parameter

space.

Defining a cutoff value of  $\text{LR}_{\text{cutoff}} = 10^7$  cuts out all remaining NHB LR values. This ensures the selection of a signal event when applying the LR method to an undefined dataset. In the context of the categorized MC data presented here, applying a cutoff value of  $10^7$  leaves 148 events or roughly 1.5% of the full  $\nu_\mu$ -CC DIS statistics and removes all background events. The results show the effectiveness of isolating signal events from the background processes under the studied conditions.

The likelihood ratio analysis method is repeated in the same manner for  $\lambda_Y$ , the LR distributions are presented in the top row of Fig. 24. The underlying behavior for the different processes is comparable to that of the  $\lambda_X$  LR distributions. One dissimilarity lies in the amount of LR values passing the same cutoff of  $10^7$ , here only seven events or roughly 0.06% of the full statistics compared to the remaining 1.5% for  $\lambda_X$ . This is likely due to the smaller separation found between the signal and background processes in  $\lambda_Y$ , as discussed in chapter 3.4 (see Fig. 13).

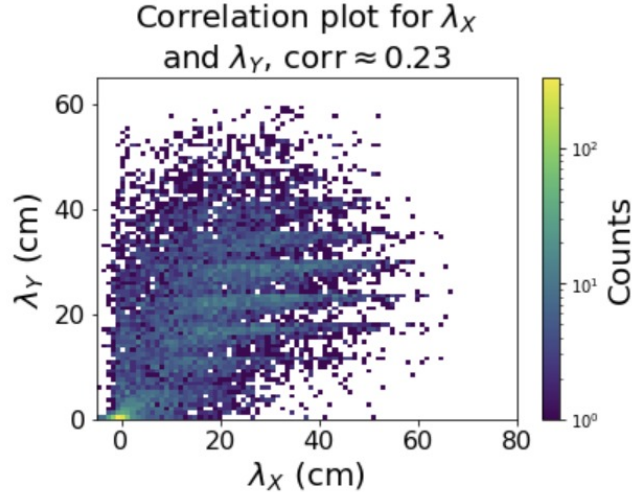


**Figure 23:** The correlation between  $\lambda_X$  and  $\lambda_Y$  is examined and a weak correlation of  $\approx 0.23$  is derived. The multivariate LR approach is thus justified in the context of this work.

In a next step, the LR methods for  $\lambda_X$  and  $\lambda_Y$  are combined to test if there is an increase in the discrimination power. For this the likelihood ratios of the individual parameters are multiplied:

$$\text{LR}_{XY} = \text{LR}_X \cdot \text{LR}_Y. \quad (13)$$

The multiplication, which is only applied in the case of independent parameters, is justified here due to the weak correlation present between  $\lambda_X$  and  $\lambda_Y$ . As can be seen in Fig. 23, a correlation of  $\approx 0.23$  is found. In the context of this analysis, aiming to merely test the introduced methods and feasibility of a combined LR application, this correlation is deemed negligible. In an expansion of this analysis, one may consider modeling the joint probability distribution of  $\lambda_X$  and  $\lambda_Y$ .

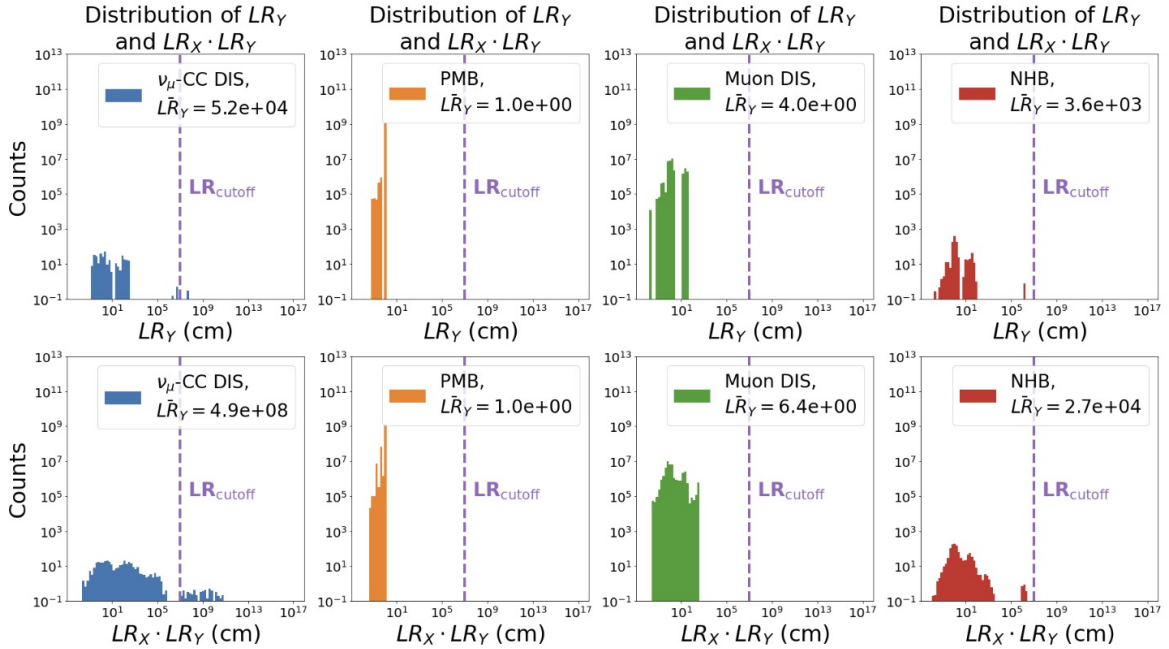


**Figure 24:** Top row: LR distributions calculated from  $\lambda_Y$  for all processes. Bottom row: combined LR distribution of  $\lambda_X$  and  $\lambda_Y$ , obtained by multiplying the likelihoods of the individual parameters.

The resulting combined LR distributions are presented in Fig. 24 (bottom row). We again observe similar behavior as with the individual LR distributions. The events passing the selected cutoff of  $10^7$  again amounts to 148 or 1.6%, comparable with the amount of remaining events in the case of  $\lambda_X$ . It follows, that combining the parameters into a single LR test, doesn't improve the overall significance. Presumably, this originates from the differing parameter ranges due to an asymmetry in the US planes in X and Y:  $\lambda_X \in [-5, 80]\text{cm}$  and  $\lambda_Y \in [0, 65]\text{cm}$ . Nevertheless, an overall increase in statistics motivates continued investigation into this method and would enhance its statistical significance.

A possibility of improving the combined LR distribution is by applying a cut on the polar

angle  $\theta < 10^\circ$  of the reconstructed muon tracks (chapter 3.5, Fig. 20), see Fig. 25. Only eight entries are left after this cut because of the lack of reconstructible muons in the NHB process, leaving only a handful of  $\theta$  values. For the  $\nu_\mu$ -CC DIS, 80 entries or  $\approx 1.9\%$  of the entire signal statistics passes the cutoff. This shows an improvement to the 1.5% when comparing to the percentage of passing events for just the  $\lambda_X$  LR distribution in Fig. 22. However, the total statistics is reduced for all processes. For example, 10435  $\lambda_X$  and 10002  $\lambda_Y$  values constitute the full set of  $\nu_\mu$ -CC DIS statistics before the  $\theta$  cut and 4054 entries remain in the combined set after the cut. The tradeoff of higher statistics for a slightly improved separation power for the signal must be carefully weighed depending on analysis goals. With larger data sets, a combined LR distribution with additional parameter cuts to exclude remaining NHB events and a possible adjustment of the penalty term represents the most promising procedure for future analysis.

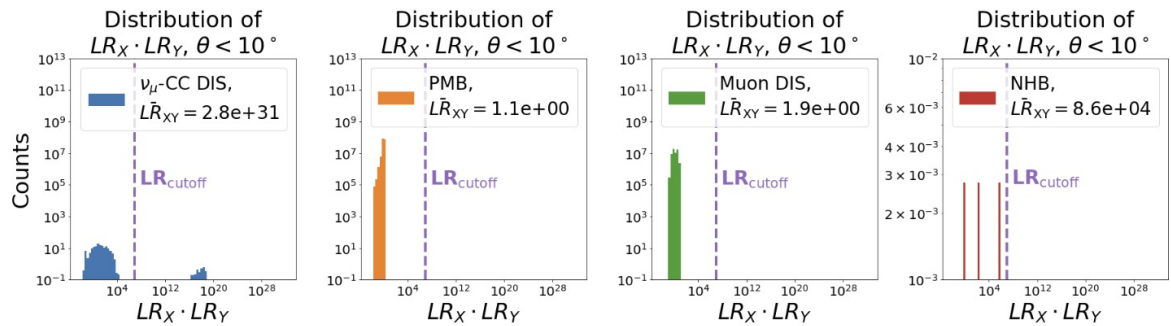


**Figure 25:** Multiple parameter ( $\lambda_X$  and  $\lambda_Y$ ) LR test with an additional cut on the polar angle of the reconstructed muon track:  $\theta < 10^\circ$ . The same LR cutoff value of  $LR_{cutoff} = 10^7$  is applied as before. Notice the differing y-limit in the NHB distribution (right).

Finally, two further parameters, the polar angle  $\theta$  of the reconstructed muon track itself and the number of SciFi hits per event, are analyzed within the scope of the LR analysis. The corresponding distributions can be found in chapter A, Fig. 44. The amount of statistics passing the LR cutoff criteria of  $10^7$  is  $\approx 4.3\%$  for the SciFi hit parameter and  $\approx 0.7\%$  for the polar angle parameter. It follows, that the former of these has the highest performance on signal separation found for any parameter so far and should be subject of further investigation. Overall, all parameters show similar behavior, supporting the chosen cutoff and penalty term values and demonstrating the validity of the proposed method.

To summarize, in this chapter a likelihood based approach of classifying events as signal or

background-like is introduced. For this, likelihood ratios are calculated using the PMFs of the respective  $\lambda_X$  distributions and subsequently a cutoff LR value of  $10^7$  is identified, allowing for the selection of signal events. This method is expanded to include the  $\lambda_Y$  distributions, assessing if combining two parameters into a single LR test increases the separation power between signal and background. The percentage of LR values passing the cutoff value for the individual  $\lambda_X$  and  $\lambda_Y$  LR distributions amounts to 1.5% and 0.06% respectively, whereas for the combined  $LR_{XY}$  distribution 1.6% of the total statistics pass the cutoff. Even though the total statistics is increased in this way, there isn't a significant improvement in the separation power. An additional cut on the reconstructed muon track polar angle  $\theta$  is applied in a next step, drastically reducing the NHB entries in a similar parameter range to the  $\nu_\mu$ -CC DIS and consequently increasing the passed statistics to 1.9%. Finally, two further parameters are introduced and analyzed in the context of the LR test: the number of SciFi hits per event and the polar angle of the reconstructed muon track. Of the total statistics, approximately 4.3% and 0.7% entries pass the  $10^7$  cutoff criteria respectively. Overall, a parameter with a strong separation power in combination with a further cut targeting remaining NHB events, while adjusting the penalty and cutoff terms, is the proposed procedure for this analysis method.

In conclusion, the proposed LR method performs best for individual parameters with an already existing separation power between signal and background. The attempt at combining parameters to increase the separation power doesn't provide conclusive results but suggests an improvement in the performance. However, multiple parameter LR distributions become increasingly complex due to possible correlations between the parameters or differing parameter spaces. Some adjustments that could be made in future analysis to possibly improve the performance pertain to the following: the penalty term, cutoff value, higher statistics or the procedure of combining multiple parameters. Nevertheless, the ability of this method to classify events into signal or background is proven, with a classification efficiency up to 4.3%. Comparing this to the efficiency of the applied cuts in chapter 3.3, Fig. 2 of 3%, indicates that the LR test method could possibly serve as an alternative to the previously employed selection cuts. A combination of the LR test and a subset of selection cuts is also feasible. The drawback of the LR test method introduced in this chapter is the necessity of a parameter with strong separation power. In chapter 4.2 an alternative method is introduced, which instead utilizes multiple parameters, each with weaker separation power, to improve the overall discrimination.

### 4.1.2 Construction of Likelihood Fits

The second likelihood based method presented in this chapter relies on the  $\lambda$  distributions introduced in chapter 3.4 and applies a defined composite model containing signal and background processes to these histograms. Next, minimizing the negative log-likelihood (nll) of the model obtains the best fit parameters, finding the most likely normalization of each component. Afterwards, the fit can be applied to run data to extract the contribution of signal and background components.

For the purpose of this analysis, the weighted raw counts of the histograms shown in Fig. 11 and Fig. 12 are used. A composite model of these histograms is defined as follows:

$$f(a, b, c, d) = a \cdot \nu_\mu\text{-CC DIS} + b \cdot \text{PMB} + c \cdot \text{muonDIS} + d \cdot \text{NHB}, \quad (14)$$

where the scaling factors  $a, b, c, d$  correspond to the relative contributions of the processes.

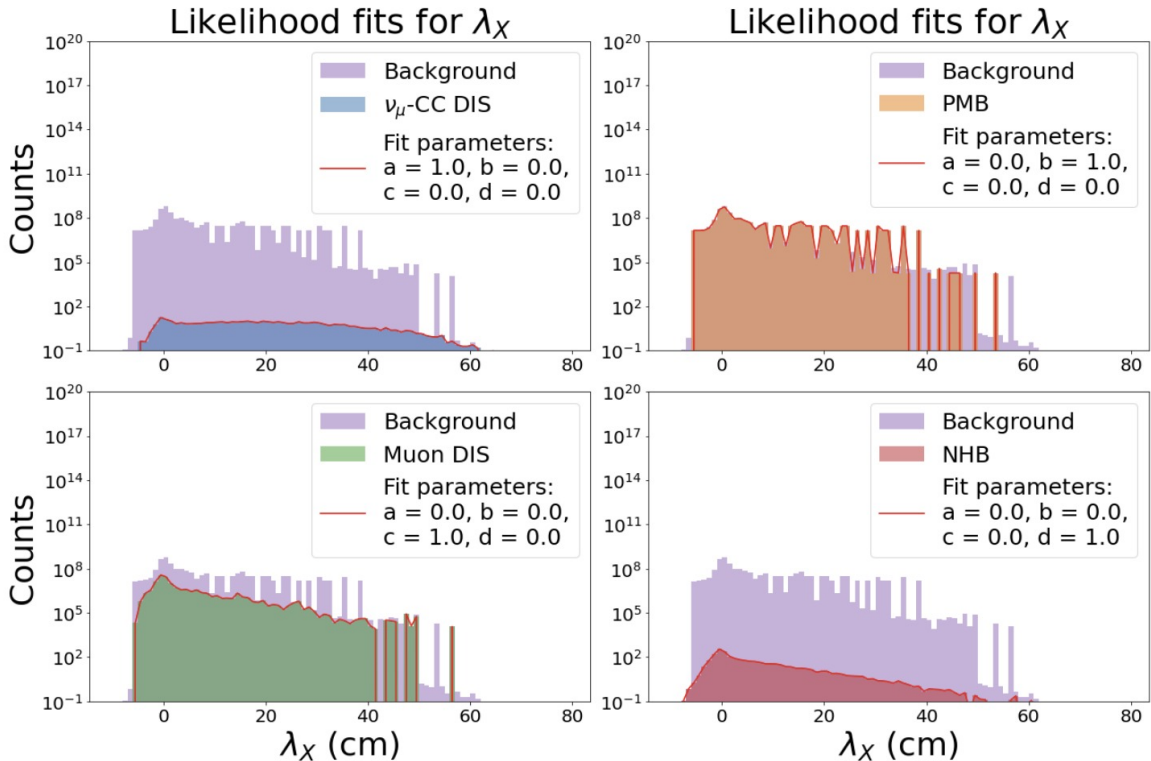


**Figure 26:** In a first step, the performance of the defined model and introduced fitting method are tested by successfully identifying the signal and background processes.

The goal of the following steps is to utilize  $a, b, c, d$  as fit parameters and optimize these for the  $\lambda$  distributions by maximizing the total likelihood  $L$ , given the model. The total

likelihood  $L$  is constructed as the product of the probabilities  $P$  of observing  $O_i$  events in bin  $i$ , given the expected number of events  $E_i$  predicted by the composite model  $f(a, b, c, d)$ :

$$L = \prod_i P(O_i | E_i). \quad (15)$$

These probabilities are obtained by assuming a Poisson distribution per bin with the mean of the distribution being the expected bin count  $E_i$ :

$$P(O | E) = \frac{E^O \cdot \exp(-E)}{O!}. \quad (16)$$

For simplicity, the negative log-likelihood is minimized in place of maximizing the likelihood  $L$ , this avoids handling the computationally expensive products in eq. 15. Using eq. 15 and eq. 16, the negative log-likelihood is calculated as follows:

$$\text{nll} = - \sum_i (O_i \cdot \log(E_i) - E_i), \quad (17)$$

resulting in the optimized fit parameters  $a, b, c, d$ . The trivial case of identifying the four contributing processes is found in Fig. 26 for  $\lambda_X$  (see Fig. 45, chapter A for the equivalent  $\lambda_Y$  plot) as a proof of concept for the defined composite model and fitting method. All processes are correctly identified; a further test is implemented and shown in Fig. 27.

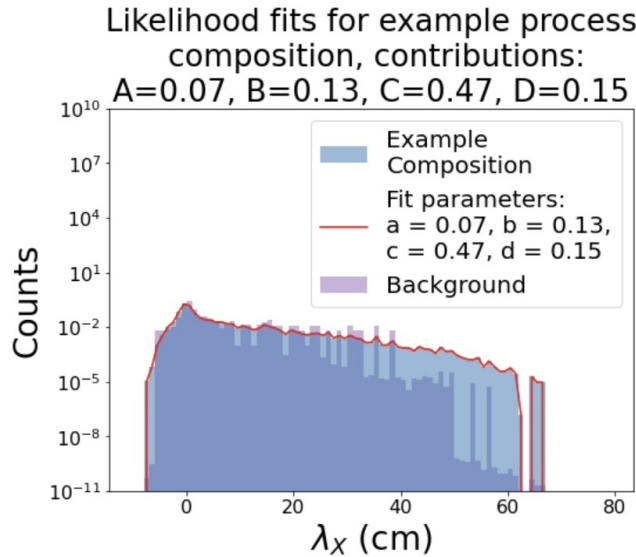


**Figure 27:** Depicted is the resulting likelihood fit of the composite model  $f(a, b, c, d)$ , with relative contributions from each of the four relevant processes. The fit parameters  $a, b, c, d$  accurately reproduce these contributions.

An arbitrarily chosen ratio of the four processes is used:  $A \cdot \nu_\mu\text{-CC DIS} + B \cdot \text{PMB} + C \cdot \text{muon DIS} + D \cdot \text{NHB}$  where  $A = 0.07$ ,  $B = 0.13$ ,  $C = 0.47$  and  $D = 0.15$ . The fit parameters  $a, b, c, d$  obtained, based on the composite model and fit method introduced above, accurately reflect the relative contributions of the signal and background processes. Here, all distributions are normalized, improving the performance of the fit.

To further evaluate the performance of the fit, the residuals between the fit parameters  $a, b, c, d$  and the relative contributions  $A, B, C, D$  are calculated. This is done iteratively 1000 times, for each iteration  $A, B, C, D$  are randomly picked from a value range of  $[0, 1]$ . The resulting distributions of residuals are found in Fig. 28 for each contributing process.

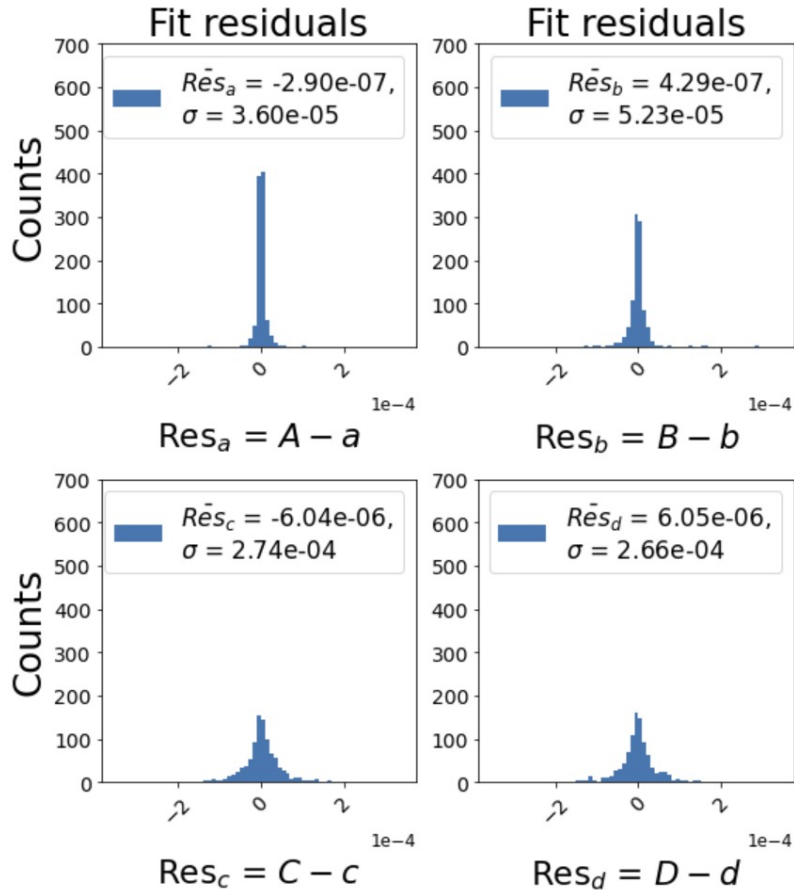


**Figure 28:** Residuals of the relative contribution parameters  $A, B, C, D$  of the four relevant processes ( $\nu_\mu\text{-CC DIS}$ , PMB, muon DIS and NHB respectively) and the obtained fit parameters  $a, b, c, d$  over 1000 iterations. The contribution parameters are randomized for each iteration from the parameter range  $[0, 1]$ .

For all contributing processes, the residuals are centered around zero, highlighting the good performance of the fit and model applied. Nevertheless, a varying spread is observed

between the different processes, with the contributions  $A$  from the signal  $\lambda_X$  distribution and the fit parameter  $a$  showing the greatest agreement and the muon DIS (C,c) and NHB (D,d) having the largest discrepancies. Possibly, these differences in the residuals originate from the shapes of the respective  $\lambda_X$  distributions. For example,  $\nu_\mu$ -CC DIS is unique with  $\lambda_X$  values ranging up to  $\approx 60\text{cm}$ . This is a less likely occurrence for the background processes, increasing the performance of the fit in this parameter range for the signal.

Overall, the application of the presented model and fitting procedure has the ability of identifying the relative contributions of the four relevant processes to a random  $\lambda_X$  distribution. As with the likelihood ratio test (chapter 4.1.1), the inclusion of further parameters in the above method to combine their individual discrimination power is subject of possible future analysis. Furthermore, the fitting procedure must be applied to run data, which is done in chapter 5. A drawback of this method, in comparison with the LR test method introduced before, is the limit of applying it to a parameter region instead of individual events. However, the likelihood fits have the advantage of providing direct estimates of physical parameters. In general, both of the likelihood based methods indicate successful identification of signal-like event or parameter regions but further improvements and validation can be made with increased statistics.

## 4.2 Boosted Decision Tree (BDT) Analysis

In this chapter a further analysis method is introduced, again with the goal of discriminating the signal  $\nu_\mu$ -CC DIS events from the background processes. For this a boosted decision tree is designed, trained and evaluated using MC data. As mentioned before, this method incorporates many parameters with lower signal-background discrimination power to combine these into an effective classifier. This alternative approach provides a solution to the lack of a single strong discriminating parameter encountered in the likelihood-based methods. Many of the parameters already introduced in previous chapters are utilized in the BDT as features in addition with further parameters, which are introduced in the following. Subsequently, the BDT model and training is introduced and its performance evaluated. The problem of applying the relevant normalization of the signal and background processes is tackled. Finally, the importance of the different features is presented and the results discussed.

The following parameters introduced in chapters 3.4 and 3.5 are incorporated into the BDT: the reconstructed interaction wall, the hadron shower width in the SciFi and HCAL  $\lambda_{X/Y}$ , the polar angle  $\theta$  and azimuthal angle  $\phi$  of the barycenters and reconstructed muon

track, as well as the projection in X and Y of the polar angle  $\theta_{X/Y}$  (see eq. 10c). Further parameters relevant for the BDT are the hit count per event in the HCAL and the SciFi, see Fig. 29 and Fig. 30 (left) respectively. On average, a  $\nu_\mu$ -CC DIS event has  $> 40$  hits more than the background processes in the HCAL and  $> 3000$  hits more in the SciFi. The large amount of hits in the SciFi compared to the HCAL can be explained with the material density in the respective detector stations. The target system consists of tungsten while the HCAL planes are made of Iron. It follows, that most interactions occur in the target system and the consequent energy deposition attenuates in longitudinal direction for all processes. Additionally, the SciFi has a higher resolution than the HCAL.

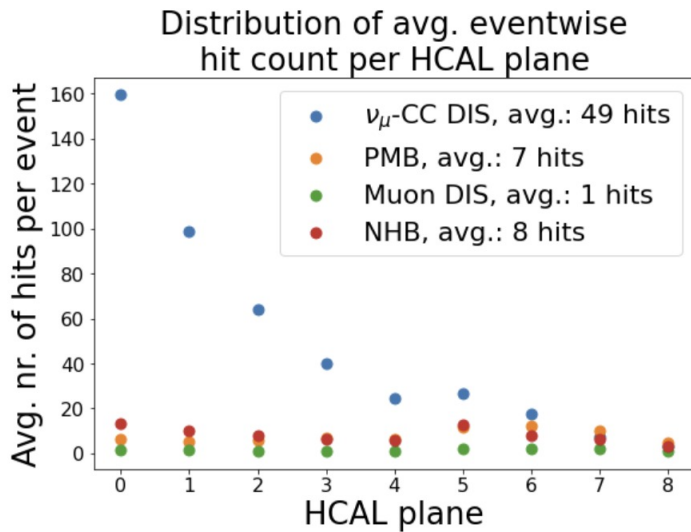


**Figure 29:** The average number of hits per event and HCAL plane depicted here shows large discrimination power between the signal (blue) and background processes, most significantly for early US planes.

Finally, the sum of the energy deposition in the US (Fig. 30, middle) and in the HCAL (Fig. 30, right) are the final two additions to the parameter set used in the BDT.

A balanced dataset is required to train and test a BDT. The issue, already observed and described in chapter 3.5, of the lack of reconstructed muon tracks for the NHB compared to the other processes arises. It follows, that events are missing parameter values obtained from the reconstructed muon track, such as the polar and azimuthal angles  $\phi, \theta$ . To circumvent the problem and an imbalance in the dataset, the datasets of the other three processes are trimmed to match the available statistics of the NHB for the BDT parameter set. A randomly picked subset of 20000 samples is thus chosen from the signal, PMB and muon DIS datasets

to match the NHB statistics. In preparation for training, the datasets are split into a training set, encompassing 80% of the datasets, and a test set with the remaining 20%. This is done using the package "Scikit-learn" [12]; the corresponding normalization weights are also split into a training and testing subset.

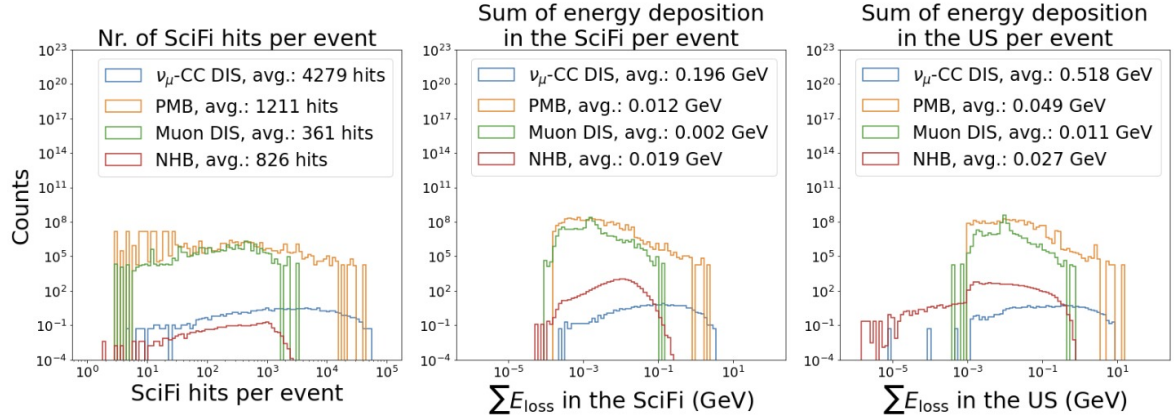


**Figure 30:** From left to right: number of SciFi hits per event, sum of the energy deposition in the US per event, sum of energy deposition in the HCAL per event. The distributions of these parameters show process dependent behavior, which is taken advantage of in the BDT.

The package "XGBoost" [13] is used to create a model for training and testing, which provides a framework for extreme gradient BDTs. This powerful and efficient implementation of BDTs constructs an ensemble classifier by sequentially adding "weaker" individual trees, each trained to minimize a specified objective function. An extreme gradient model is chosen for its reliability and its out performance of the alternative "Random Forest" model. A multi-class log loss is used as the objective function to be minimized and evaluated after each round of boosting and the softmax function converts the raw output score of the BDT into probability scores. Furthermore, a learning rate of 0.1, a max depth of 7 per tree and 10000 boosting rounds are chosen. Per boosting round, a fraction of 0.9 of the training data is used to introduce diversity between the trees and avoid overfitting.

Once the model is trained and tested, the performance can be visualized using a confusion matrix (CM) as portrayed in Fig. 31. This summarizes the classification by plotting the "real label" against the "predicted label". Four different quantities of classification are determined: True Positive (TP), True Negative (TN), False Positive (FP) and False Negative (FN). Subsequently, the precision, recall, f-score and accuracy can be defined from these quantities.

The precision quantifies the accuracy of the positive predictions whereas the recall reflects the model's ability to correctly identify all instances of a certain class.

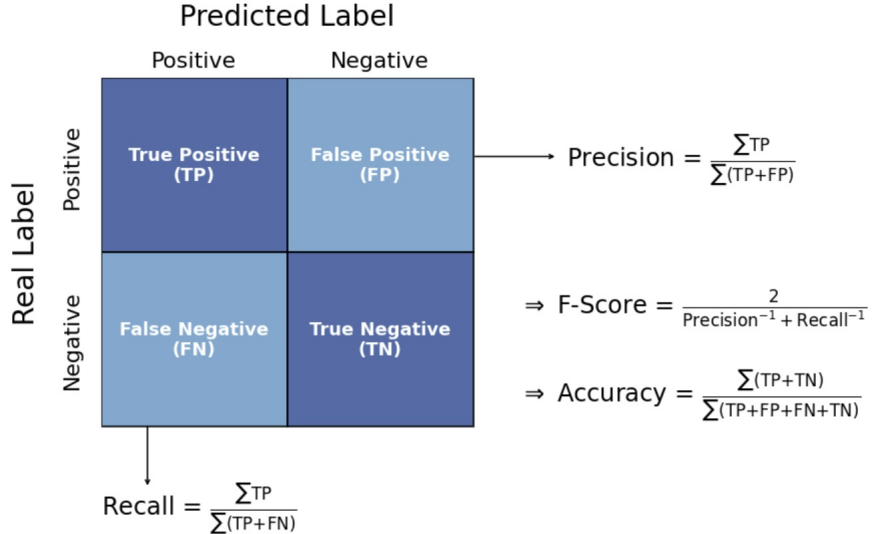


**Figure 31:** Diagram of the components of a confusion matrix, used to visualize the performance of a BDT. Relevant definitions depicted are the precision, recall, f-score and accuracy.

Utilizing the precision and recall, the f-score is defined as the harmonic mean of these two quantities and measures the class-wise performance of the model. The accuracy is defined as the ratio of correctly classified samples (diagonal elements) to the sum of all samples and measures the performance of the model over all classes. The accuracy must be taken with caution though in the case of imbalanced data sets, which will become an issue later in the chapter when applying the normalization weights to the confusion matrix. It is then advised to fall back on the precision, recall and f-score to evaluate the performance of the BDT per class.

The confusion matrix of the trained and tested BDT is presented in Fig. 32 (left). The CM is not yet weighted to the integrated luminosity of  $L = 36.8 \text{ fb}^{-1}$ , only the raw output is depicted to first evaluate the performance of the BDT on a balanced dataset. From the diagonal elements, it is evident, that many samples are classified correctly. However, there are several instances of misclassification that need to be investigated. The largest misclassification of the signal is as PMB, due to several possible interactions for a passing muon in the detector, that could mimic a hadron shower: delta ray emission, Bremsstrahlung and lepton pair production.

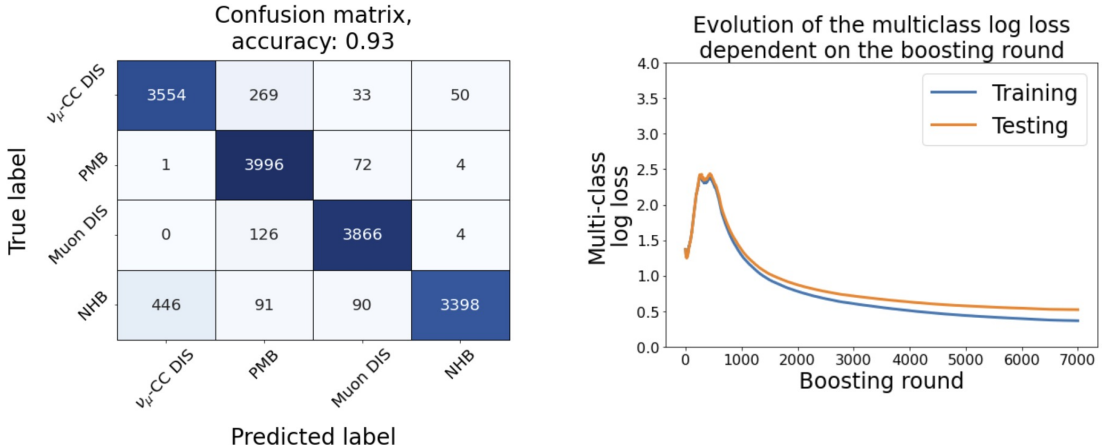


**Figure 32:** Left: confusion matrix to visualize the performance of the BDT on the different classes, an accuracy of 0.93 is achieved. Right: loss curve of the BDT over 7000 boosting rounds for training and testing; the multi-class log loss is chosen as the objective function to minimize.

Additionally, the SciFi hit count (Fig. 30, left) and SciFi energy deposition (Fig. 30, middle) per event of the PMB overlaps with the parameter region of  $\nu_\mu$ -CC DIS events. Furthermore, the largest overall misclassification occurring is of NHB samples as signal events. This is not surprising due to observations made in previous chapters pertaining to the  $\lambda$  (chapter 3.4, Fig. 13) and polar angle  $\theta$  distributions (chapter 3.4, Fig. 16 and chapter 3.5, Fig. 20). The large hadron shower width and polar angle, as well as the large polar angle of the reconstructed muon track found in the signal distributions are mimicked by the presence of high-energy neutral hadrons producing wide showers and large-angle scattering in the NHB. Finally, muon DIS samples being misclassified as a passing muon event make up the third largest contribution to misclassifications. In the muon DIS MC files, the primary muon is forced to undergo DIS in the cavern rock upstream of the detector. The resulting signature in the detector quickly dissipates with longitudinal progression, sometimes being fully contained in the target system and leaving no trace in the HCAL. Subsequently, only the outgoing muon of this interaction is detected and would be indistinguishable from a passing muon event, for example for the muon track reconstruction algorithm. However, this misclassification of background events is less relevant for the purpose of this thesis but could be analyzed in future analysis - for example to isolate muon DIS samples. Overall though, the BDT performs well and an accuracy of 0.93 is achieved. Looking at the loss curve in Fig. 32 (right) confirms the high performance. After initial fluctuations, the training loss curve stabilizes around 0.5 in later boosting rounds while the testing loss curve only shows a

slight deviation from this, indicating a good generalization of the BDT to testing data and no significant overfitting. Possibly, an early stopping parameter could be added to find the ideal number of boosting rounds for improved performance.

To further evaluate the performance of the BDT on the individual classes, the classification report found in Fig. 33 is examined. For the most part, the observations made in the CM are reflected here. The misclassification of the NHB as signal events is reflected in the recall, of the signal as PMB in the precision and of the muon DIS as PMB also in the precision.

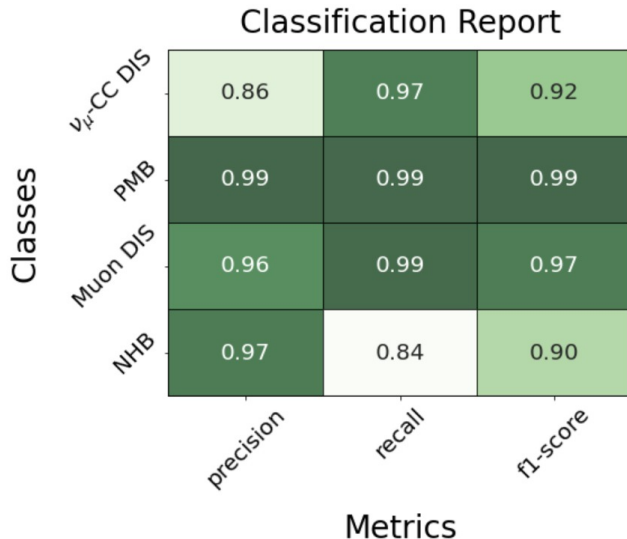


**Figure 33:** The classification report of the BDT displays the precision, recall and f-score for each class. This allows for a class dependent examination of the BDT performance. For all classes, a f-score of  $> 0.90$  is achieved.

For the signal, a recall of 0.97 signifies, that almost all signal events are correctly identified and the f-score of 0.92 indicates a good performance of the BDT with respect to  $\nu_\mu$ -CC DIS. The precision, corresponding to the samples falsely classified as signal, have the greatest impact on the BDT performance with respect to  $\nu_\mu$ -CC DIS interactions. Of the 448 samples misclassified as signal events (first columns in Fig. 32 left), 446 of these belong to the NHB class. It follows, that improvements should be made in discriminating NHB and signal to increase the f-score of the BDT for the signal. Even when examining the class dependent performance of the BDT, a f-score of  $> 0.90$  is achieved for each class and further supports the reliability of the BDT to successfully classify the signal and background samples.

To scale the BDT output to the chosen integrated luminosity of  $L = 36.8 \text{ fb}^{-1}$ , the normalization weights introduced in chapter 3.2.2 must be applied to the CM. When introducing

the weights, an imbalance in the dataset is produced in consequence of the large passing muon yield ( $O(10^8)$ ) compared to the  $\nu_\mu$ -CC DIS yield ( $\approx 10^2$ ). As mentioned earlier in this chapter, a large imbalance can introduce a bias into the accuracy towards the larger dataset. This is evident and confirmed in the weighted confusion matrix, Fig. 34 (left), where an accuracy of 0.98 is calculated even though significant misclassifications are apparent. Here, the classification report in Fig. 34 (right) has to be consulted to reliably evaluate the performance of the BDT.

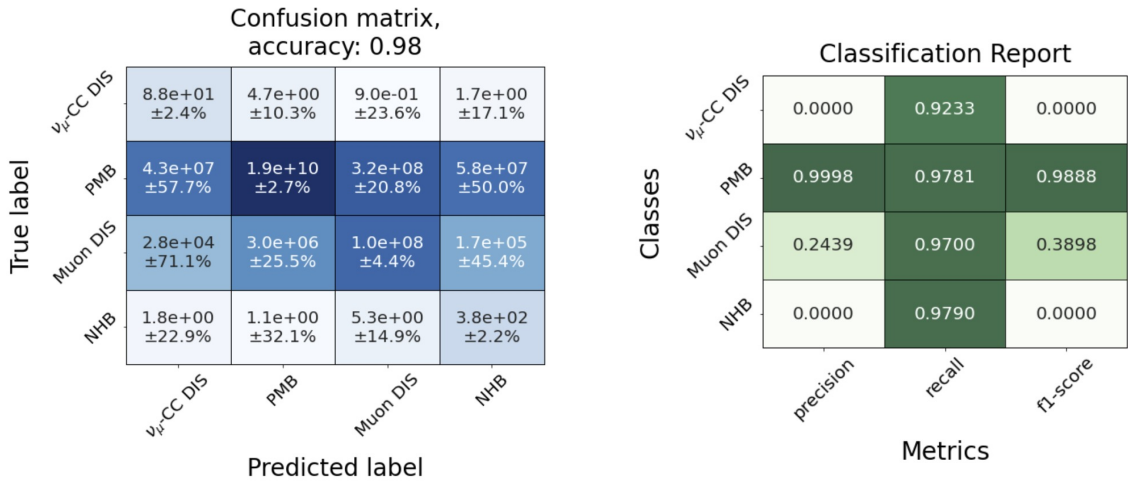


**Figure 34:** The confusion matrix (left) with implemented normalization weights shows a dominance of PMB and muon DIS events. A closer look at the classification report of the weighted BDT (right) is necessary to evaluate the performance on the individual classes.

The classification report reveals a poor performance of the BDT both for  $\nu_\mu$ -CC DIS and NHB samples. Both have a high recall of 0.92 for the signal and 0.98 for NHB, meaning a high percentage of these samples are correctly identified. However, a precision of 0.00 is recorded for both classes and indicates that a large number of samples are falsely classified as signal or NHB events resulting in a large amount of FPs. The CM confirms this observation, for example  $4.3^7 \pm 57.7\%$  PMB samples are falsely classified as signal events and  $5.8^7 \pm 50.0\%$  as NHB events. A large misclassification of  $\approx 10^4 - 10^5$  muon DIS samples also contribute to the low precisions. The PMB class dominates over the signal and NHB class by  $10^7 - 10^9$ , thus an accurate and reliable identification of signal and NHB events is not possible under these circumstances.

A further look at the CM and classification report shows also a large amount of events from the muon DIS class in the range of  $10^4 - 10^8$ . The classification report again shows a high

recall for the muon DIS and a low, but non-zero precision of  $\approx 0.244$ . All classes contribute to the misclassification as muon DIS events, where the PMB has the largest contribution of  $3.2^8 \pm 20.8\%$  but is comparable with the amount of correctly classified muon DIS events of  $1^8 \pm 4.4\%$ . It is conceivable, that a repurposing of the BDT tailored to the muon DIS process could improve the performance for this class. A separation of the PMB and muon DIS would be the goal in this case and significantly help the cause of an energy calibration of SND components.

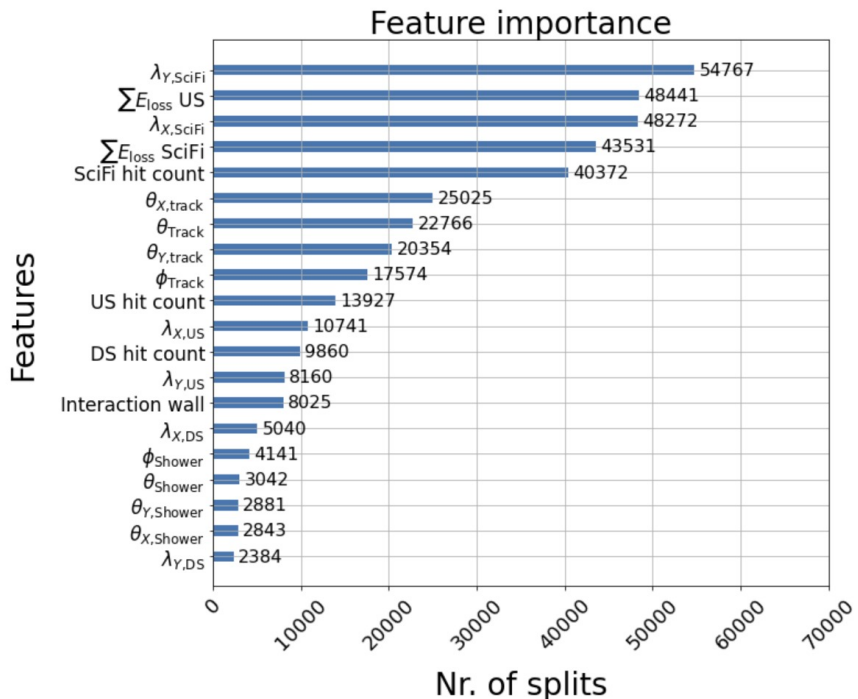


**Figure 35:** Depicted are the features incorporated into the BDT in order from most (top) to least (bottom) important for the classification. This is determined by how often a feature is used to split a tree to achieve the highest possible gain at each split.

In summary, the high recall found for all classes reflects the high performance of the BDT as seen before in the case of the unweighted CM. The dominance of the PMB makes a classification of  $\nu_\mu$ -CC DIS events under the presented circumstances impossible. Nevertheless, valuable information can be gleaned from the BDT by looking at the features incorporated and their importance during the classification process as depicted in Fig. 35.

The features with the largest importance are the SciFi shower width in X and Y. This large importance can likely be traced back to the  $\nu_\mu$ -CC DIS interactions originating in the target system and causing large activity in the SciFi compared to the background processes. Coupled

with the high resolution in the SciFi, this activity is the reason for the high discriminating power of  $\lambda_{\text{SciFi}}$ . The importance of the SciFi hit count can be explained in the same way. Furthermore, the sum of the energy deposition per event in the US and SciFi have a high feature importance, likely due to the characteristic signal hadron shower being contained in these systems whereas the background processes don't have comparable energy depositions. The high discrimination power of  $\lambda_{X/Y,\text{SciFi}}$  and of  $\sum E_{\text{loss}} \text{US}/\text{SciFi}$  have potential with respect to the likelihood ratio test in chapter 4.1.1 and likelihood analysis in chapter 4.1, which utilize individual parameters to classify signal events. The original parameters used, the shower width in the US  $\lambda_{X/Y,\text{US}}$ , are found lower in the feature importance list. The lower discrimination power of this parameter is possibly explained by the lower resolution found in the US planes, which should be increased if possible in future improvements of the SND experiment.

To summarize, in this chapter further parameters are introduced to be used as features with discriminating power between signal and background: the hit count per event in the SciFi and HCAL and the sum of the energy deposition per event in the SciFi and HCAL. A BDT is modeled, trained and tested on a set of data consisting of 20k samples per class. A high accuracy of 0.93 is achieved for an unweighted BDT, where the f-score ranges from 0.90 – 0.99 over all classes. Despite the capability of the BDT to successfully classify signal events, misclassifications of signal samples as PMB and of NHB samples as signal events occur and should be investigated in future analysis. Adding the normalization weights introduces a large bias of the BDT towards PMB, where this process dominates over the other process samples by  $10^2 - 10^9$ . Thus, the weighted BDT can not classify  $\nu_\mu$ -CC DIS events, as confirmed by the f-score of 0. However, an f-score of  $\approx 0.39$  for the muon DIS indicates the possibility of repurposing and tailoring the weighted BDT to separate the muon DIS from PMB. The features used in the BDT and their importance are analyzed. It is determined, that the hadron shower width in the SciFi  $\lambda_{X/Y,\text{SciFi}}$  and the total energy deposition in the SciFi and US  $\sum E_{\text{loss}} \text{SciFi}/\text{US}$  have the highest feature importance. It follows, that they have the largest discrimination power, whereas the shower width in the US  $\lambda_{X/Y,\text{US}}$  lies farther down in the feature importance list. Therefore, the implementation of the former two parameters into the LR test (chapter 4.1.1) and likelihood fits (chapter 4.1) instead of  $\lambda_{X/Y,\text{US}}$  is recommended.

### 4.3 Summary

The previous chapter introduced three approaches to classify signal events: two likelihood based methods and a gradient BDT. These are discussed in the following.

The first likelihood based method introduced aims to classify individual events as signal or background. It utilizes PMFs obtained from  $\lambda$  distributions, finds the probability of events being signal or background and builds the ratio of these probabilities. A cutoff term of  $10^7$  is defined. The LR test for  $\lambda_X$ ,  $\lambda_Y$  and the combination of these two distributions results in 1.5 – 1.9% of the statistics passing the cutoff criteria and successfully being identified as signal. The hit count in the SciFi and the polar angle  $\theta$  of the reconstructed muon track are also examined and these identify 4.3% and 0.7% of signal events. It goes to show, that the choice of input parameter with a high discriminating power is essential for a high performance of this method. Altogether, this method shows a high efficiency of up to 4.3%, compared to the 3% of the selection cuts while also being able to implement the normalization weights.

The second likelihood based method defines a composite model consisting of all four processes:  $a \cdot \nu_\mu\text{-CC DIS} + b \cdot \text{PMB} + c \cdot \text{muon DIS} + d \cdot \text{NHB}$ , where  $a, b, c, d$  are fit parameters. The likelihood  $L$  of a given distribution is maximized given the model to find the parameters and thus the relative contributions of each process. The fit is tested by iterating over 1000 randomly chosen compositions of the four processes and calculating the residual. Narrow distributions of the residual centered around 0 indicate a well performing fitting method and proves the reliability of this method, while not requiring the normalization weights as only the shapes of the distributions are taken into account. Further tests could examine the performance under these conditions.

The third method, introducing a gradient BDT, avoids the necessity of a single parameter with high discrimination power and instead combines the weaker discrimination power of several parameters. The BDT is modeled, trained and tested on MC data and results in an accuracy of 0.98 and an f-score of  $> 0.90$  over all classes. Some misclassifications of the signal occur and could be a good starting point when attempting to increase the accuracy. However, when the normalization weights are added to the BDT, the performance of the BDT for the signal and NHB classes is 0. The dominance of the PMB class hinders a classification with this method. A repurposing of the BDT as a classifier of PMB and muon DIS is conceivable. The feature importance of the BDT reveals that the shower width in the SciFi  $\lambda_{X/Y,\text{SciFi}}$  and the total energy deposition in the SciFi and US have the highest discrimination power between signal and background. Even though the BDT can't single-handedly classify signal

events, it could be used in combination with subset of selection cuts and is worth being analyzed in future analysis. Possibly the pre-selection, fiducial and veto cuts would suffice.

Distinguishing between  $\nu_\mu$ -CC DIS and NHB is the largest source of errors or misclassification for both the LR test and the BDT. It follows, that the efforts of this work could be refocused into extracting the signal from NHB. The PMB and muon DIS can be largely suppressed through the extended veto cuts and are also easily distinguishable from the signal through the behavior of many of the parameters examined here.

All in all, the likelihood fits show the most promising results and are suggested to be used as a classifier for signal events. The performance of the BDT on MC data is very high until the normalization weights are applied. It is suggested to implement a subset of selection cuts to reduce the background contamination before applying the BDT.

## 5 Comparison with Run Data

In this chapter some of the simulation components, such as the spatial analysis of the hadron shower in the HCAL or the likelihood based classification methods, are applied to run data and compared with the previously discussed MC data. The  $\nu_\mu$ -CC DIS events identified in [2] are taken for this purpose. Additionally, eight further events are utilized, which undergo relaxed selection cuts: 2nd and 5th interaction wall no longer excluded and an updated tracking algorithm. The relaxed cuts are also applied to the MC data. In total, 16 events are extracted from run data to be used in the following. The comparison should be taken with caution due to the limited statistics.

Firstly, the hadron shower position is calculated similarly to the method presented in chapter 3.4, eq. 5a. Differences arise due to the time alignment of the HCAL and corrections applied to counteract time walk effects, see [10] for details. Furthermore, the relative energy deposition weighting found in eq. 7 is omitted for run data. The resulting barycenter distributions in X and Y for run data and MC data are depicted in Fig. 36 for all US planes. The shape of the distributions in both X and Y for MC behave similarly: peaked distributions centered around an average of  $-22.91$  cm and  $32.72$  cm respectively and an attenuation of the hadron shower resulting in less hits and more uniform distributions in later US planes. There is no significant fluctuation of the mean X and Y barycenter  $\bar{x}_B$ ,  $\bar{y}_B$  in either run or MC data throughout the US planes. The  $x_B$  distribution for run data shows comparable behavior of a peaked distribution in the first US plane, which diffuses to a more uniform distribution in later planes.

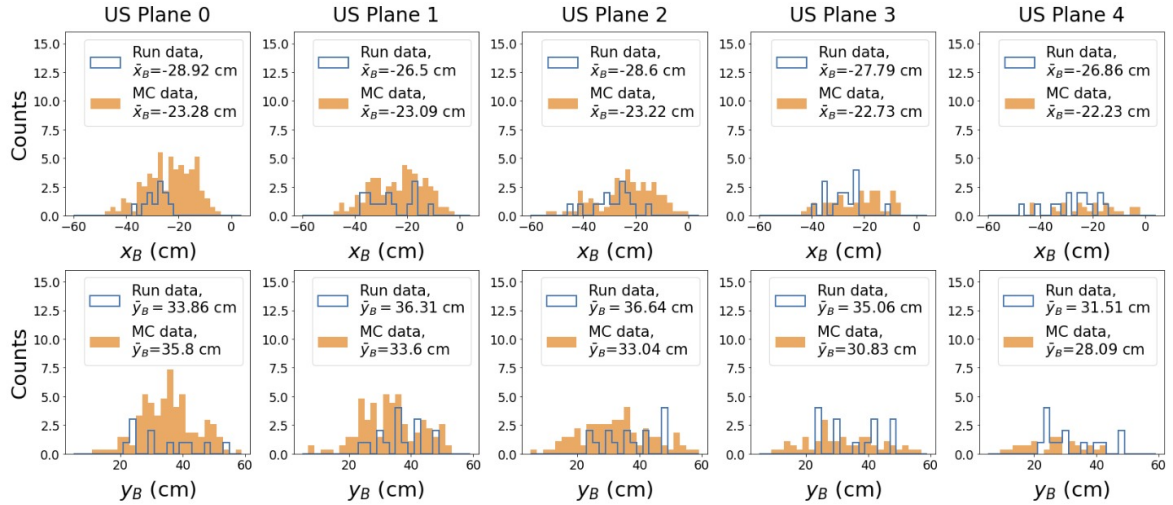


**Figure 36:** Comparison of the barycenters  $x_B$ ,  $y_B$  between run data (blue) and MC data (orange) per US plane. The average of  $x_B$  over all US planes is:  $-22.91$  cm for MC data and  $-27.73$  cm for run data. For  $y_B$  the averages are  $32.72$  cm and  $34.68$  cm for MC and run data.

However, the histogram counts seen in Fig. 37 reveals, that the same attenuation of the hits isn't present in run data but is instead just a redistribution of hits over the parameter range.

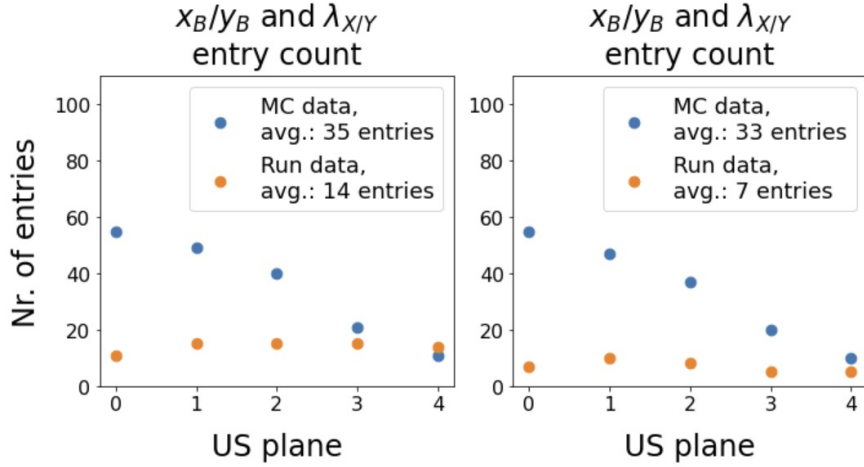


**Figure 37:** Entry count of the barycenter and  $\lambda$  histograms (Fig. 36 and Fig. 38) per US plane. A linear decline corresponding to the attenuation of the hadron shower in the US is observed in MC data but not in run data.

This discrepancy could arise from the energy loss threshold of 1 MeV chosen per DS bar in the pre-selection cuts (Table 2). Possibly, the energy deposition necessary for a hit to be

detected in the HCAL is lower than set in the MC and disproportionately affects the early US planes.

In Y there is no discernible underlying behavior of the run data  $y_B$  distributions, the barycenters are approximately uniformly distributed over the parameter range for all US planes. However, column structures are visible in the distributions corresponding to the scintillator bar positions in Y. The structures are not found in the MC data because of the multiplication of the bar positions with their relative energy deposition. In future analysis it is advised to adjust the methods and apply the same procedures for both MC and run data. The average barycenters throughout all planes for the run data is  $-27.73\text{ cm}$  in X and  $34.68\text{ cm}$  in Y; the difference to the MC data is about  $\Delta x_B \approx 5\text{ cm}$  and  $\Delta y_B \approx 2\text{ cm}$  in each US plane. It is conceivable, that the reason for the difference in Y lies in the slightly varying methods of calculation. Further reasons could be the energy loss threshold chosen for the MC, residual time-walk effects or detector inefficiencies. Overall, a decent agreement is found between the barycenter calculation for MC and run data - considering the lack of statistics for run data - but further adjustments and investigations are necessary to improve the consistency.

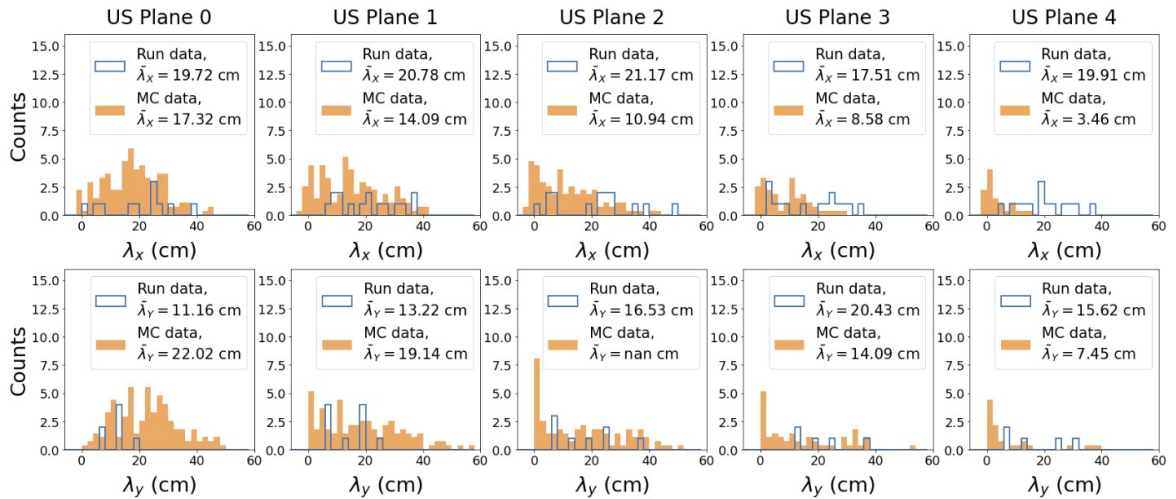


**Figure 38:** Distributions of the shower width  $\lambda$  in X and Y for run data and MC data per US plane. The average  $\lambda$  value and longitudinal development are found in Fig. 39.

The shower width for the run data is also calculated as in [10] and compared with the MC distributions in Fig. 38. Again the  $\lambda$  distributions attenuate for the MC data with increasing US plane. The same discrepancy between the MC and run data in the histogram entry count

is found for  $\lambda$  in Fig. 37 (right) as before. The shape of the  $\lambda_X$  MC data distribution is more broad and centered around the mean value for earlier US planes and becomes narrower and peaked at 0 cm for later US planes. A similar trend in the shape of the run data is difficult to discern due to the lack of statistics. An expected attenuation of the hadron shower within the HCAL and resulting peak at 0 cm indicates, that the method of defining the hadrons shower width in the MC is able to replicate some key aspects of the  $\nu_\mu$ -CC DIS interactions. The question is rather, if the sensitivity or resolution of the detector is too low to resolve this underlying trend. A closer look at the development of the distributions is given in Fig. 39, where the average  $\lambda_{X/Y}$  values per US plane are portrayed.

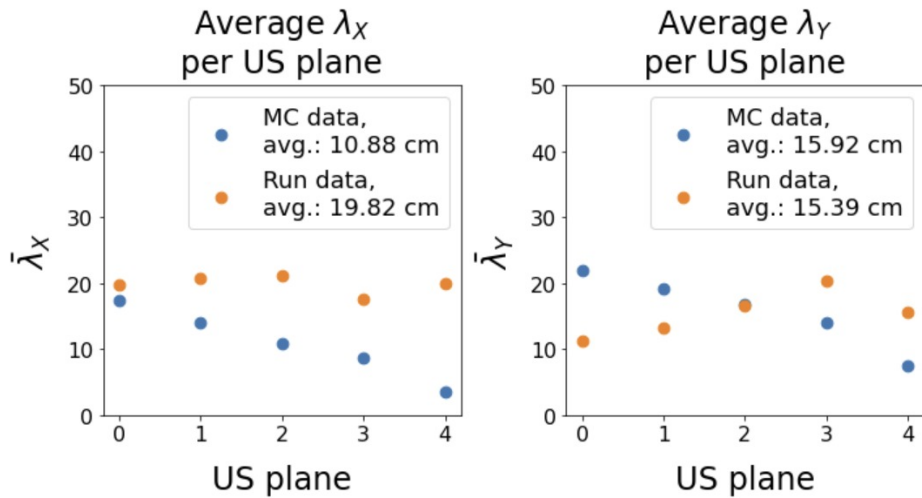


**Figure 39:** Development of the average  $\lambda_x$  and  $\lambda_y$  values through the US planes for both run and MC data. An attenuation is observed for the MC data but not for the run data.

The average  $\lambda_X$  value over all US planes is  $\bar{\lambda}_{X,MC} = 10.88$  cm for MC data and  $\bar{\lambda}_{X,run} = 19.82$  cm for run data. For Y these averages are  $\bar{\lambda}_{Y,MC} = 15.92$  cm for MC data and  $\bar{\lambda}_{Y,run} = 15.39$  cm for run data. As with the barycenter, the values in Y are comparable between run and MC data but a difference of  $\approx 9$  cm is found in X, possibly due to reasons already stated above. Similarly, a linear decline of  $\lambda_X$  and  $\lambda_Y$  is given in the MC data where the run data stays more or less constant throughout the US planes. It is apparent, that there are several discrepancies found between run and MC data both in the barycenters  $x_B/y_B$  and the shower width  $\lambda_{X/Y}$ . The lack of statistics limits the possibilities of the comparison and also the ability to identify potential errors.

Next to the spatial characterization of the hadron shower in the HCAL, the likelihood based analysis methods introduced in previous chapters (see chapters 4.1.1 and 4.1) is also

applied to run data. The results of the LR test are presented in chapter A, Fig. 46, where the run data is depicted in blue and the background MC processes in orange (PMB), green (muon DIS) and red (NHB). None of the signal events pass the cutoff criteria of  $\text{LR}_{\text{cutoff}} = 10^7$ . This behavior is unexpected and not understood. Further investigation is being performed to adjust the LR test method.

In Fig. 40, the application of the likelihood fit to run data is presented. Here the MC data is still used as a template for the model, as done in chapter 4.1. Despite the lack of statistics, the fit accurately identifies the input distribution as fully belonging to the  $\nu_\mu$ -CC DIS process. This initial test on run data shows promising results and must be validated when further statistics are available and with samples from background processes. Furthermore, the  $\lambda_X$  parameter could be substituted for one with higher signal-background discrimination power, as identified in chapter 4.2.

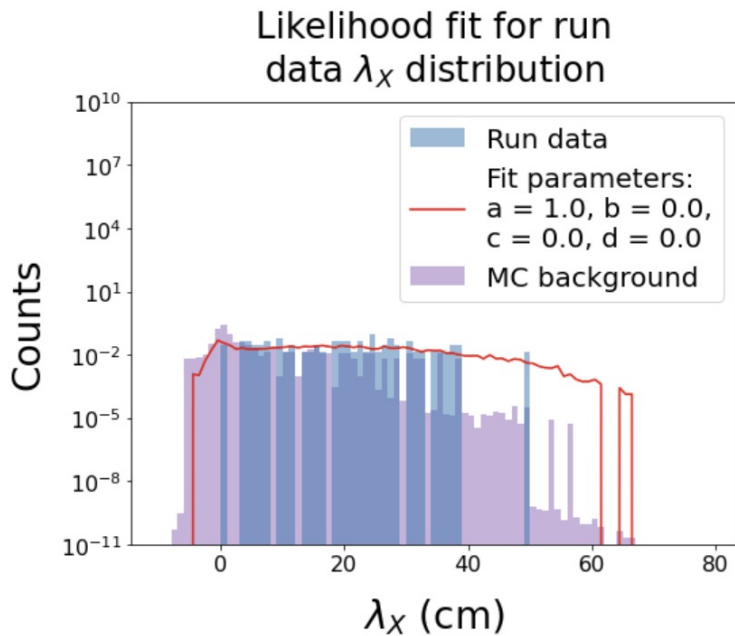


**Figure 40:** The likelihood fit introduced in chapter 4.1 for  $\lambda_X$  is applied to run data, the fit successfully identifies this distribution as being signal.

To recapitulate, this chapter applies the hadron shower characterization (chapter 3.4) and the likelihood based methods (chapters 4.1.1 and 4.1) to 16  $\nu_\mu$ -CC DIS events extracted from run data. The lack of statistics warrants a careful approach and interpretation of the results. A comparison is made with the distributions of the equivalent MC data. Comparing the barycenter  $x_B/y_B$  and shower width  $\lambda_{X/Y}$  between run and MC data shows similarities

in shape and values. However, an expected attenuation of the hit counts with increasing US plane is found in the MC data but not in the run data. This leads to the following questions that must be investigated in future: is the energy loss threshold set in the pre-selection cuts for the MC too high, is the detector sensitivity too low, should the hadron characterization methods be adjusted to mimic lower sensitivity? In general, the comparison indicates that the defined barycenter and  $\lambda$  methods are a good description of the real hadron shower position and width.

The likelihood based methods are tested on the run data as well. An LR test fails to identify the signal events from the run data. The reason for this poor performance is not found. Nevertheless, due to the good performance of the LR test on MC data, this analysis methods should not yet be excluded as a possible classification method. The second likelihood based method - likelihood fits based on MC  $\lambda_X$  distributions - correctly predicts the distribution from run data as belonging to  $\nu_\mu$ -CC DIS. Further validation is desired, for example with background samples from run data. However, this method seems to be the most feasible and efficient for classifying signal run data.

To summarize, similar values and shapes are found in the barycenter  $x_B/y_B$  and shower width  $\lambda_{X/Y}$  distributions between run and MC data. A difference is observed in the evolution of the hit count in the US: an attenuation is found for MC data but not for run data. Possibly the detector, specifically the HCAL, is more sensitive to incoming particles and records more hits in the later US planes than in the MC. Certain aspects of the simulation, such as the energy deposition threshold (Table 2, cut 1), could be adjusted to test this. The LR test method doesn't result in any correctly identified signal events. On the other hand, the likelihood fits utilizing the MC processes as a base can correctly identify the signal  $\lambda_X$  distribution. Even though the LR test didn't perform well on run data, the performance on MC data promises to be more efficient than the previously used selection cuts. The lack of run data statistics further supports that the LR test shouldn't be excluded quite yet. The application of some of the simulation and analysis methods to run data is deemed as successful even though a thorough comparison of the performance to MC data isn't possible due to the lack of statistics.

## 6 Conclusions and Outlook

Throughout this work, the goal is to contribute to the efforts of the SND collaboration of achieving a higher classification efficiency for  $\nu_\mu$ -CC DIS interactions. As of now, only 8  $\nu_\mu$  candidates have been identified, whereas the expected yield for the same time period is  $157 \pm 37$ . This disparity arises due to the large amount of background events occurring in the detector in the form of passing muon background, muon DIS and a neutral hadron background. The simulation studies performed in this work aim to study the spatial development of signal events in the HCAL of the detector and find methods of characterizing this using MC data. These same methods are also applied to MC datasets of the background processes and the results are compared. In this way, differing behavior between the different processes can be taken advantage of to attain an improved signal-background discrimination and retain more statistics from the run data. A series of analysis methods is also introduced for this purpose. A brief comparison with run data seeks to evaluate and compare the performance of the methods used. Through this, one could possibly detect issues in the simulation studies or gain information about the detector behavior.

Key findings in this work pertain to the characterization of the spatial development of  $\nu_\mu$ -CC DIS interactions. Several parameters are identified that show varying behavior between the different processes: the hadron shower width and polar angle as well as the polar angle of the reconstructed muon track. Additionally, an attenuation of the hadron shower depending on the interaction wall and the US plane is observed. The likelihood based analysis methods introduced also support the discrimination power of the mentioned parameters. These methods successfully utilize the hadron shower width in the US, combined in some cases with the polar angle, to classify signal events or signal-enriched parameter regions.

While implementing a gradient BDT as a classifier, several more parameters with discrimination power between signal and background are found. The examination of the feature importance of the BDT allows for an evaluation or ranking of these parameters in order of discrimination power. It is observed, that the previously used hadron shower width in the US ranks lower on this list. Instead, the hadron shower width, total energy deposition and hit count in the SciFi as well as the total energy deposition in the US emerge as the top performers. This indicates that the SciFi system is more relevant for the classification than the HCAL, specifically the US. All processes attenuate with longitudinal progression through the detector and initial assumptions were that the planes in the HCAL would record more activity for the signal than the background processes. This seems to be the case for the muon

DIS, however the PMB and NHB still show activity in the later US planes and DS and thus mimic signal behavior. The activity of PMB in the HCAL, beyond a simple outgoing muon, is explained through processes such as Bremsstrahlung, lepton pair production and delta ray emission. The presence of NHB events is especially inconvenient as this background is often found in the same value range as the signal for many of the parameters examined throughout this work. Misclassifications of the NHB as signal and of the signal as PMB in the unweighted CM of the BDT further support these observations. It goes to show that the background processes, especially NHB, can often mimic signal behavior in the HCAL and refocusing on the SciFi system is advised.

In general, the BDT works well in the case of the unweighted CM, proving the efficiency of combining the discrimination power of a set of parameters to be used for classification. Adding the normalization weights to the CM induces an imbalance between the processes. The PMB dominates and makes a classification of the signal impossible, though adding the veto cut is a conceivable solution to this issue. However, the statistics remaining after implementing this cut in the MC data are not large enough to utilize in further analysis.

An observation made with respect to the comparison of the hadron shower width between MC and run data is the lack of an attenuation for the latter. The lack of statistics for the run data makes this observation statistically inconclusive. Nevertheless, a hypothesis is put forth as a seed for further investigation. For example, the detector could possess a higher sensitivity to incoming particles than modeled in the simulation. This could be tested by decreasing the energy deposition threshold set for the MC data or by adjusting the hadron shower characterization method to be more sensitive to outlying particles.

The final important finding relates to the selection cuts, specifically the extended veto cut. It is found, that adding the first two SciFi stations to the veto doesn't increase the signal-to-background ratio. Instead, statistics are cut approximately equal across the board, meaning the extended veto is superfluous for the goal of isolating signal events. The suppression of the background processes after the pre-selection, fiducial and veto cuts are already significant, where only the NHB process still makes a notable contribution. In this work, the conclusion is made that the remaining cuts - the  $\nu_\mu$  selection cuts - can be reduced in favor of the discriminating parameters found together with one of the analysis methods introduced. A comparable or improved efficiency is suggested by preliminary results and a concrete classification strategy should be topic of a more focused study.

A complete performance evaluation of all simulation components and analysis strategies

is not possible in this work due to limitations in the available statistics. For example, the MC statistics are not sufficient enough to apply all selection cuts and still have statistical importance. Limiting the amount of cuts applied allows for larger datasets. But even so, in certain analysis the application of the track reconstruction algorithm to obtain certain parameters drastically reduces the statistics. Furthermore, the limited dataset of run data prohibits or severely impacts the comparison of the introduced methods for example the hadron shower width characterization. An increase in statistics would improve the evaluation and reliability of the results.

Overall, the work presented here confirms that there is discrimination power to be found between signal and background in the spatial analysis of the HCAL. However, it is found that the parameters obtained from the SciFi - such as the total energy deposition, hit count or hadron shower width - are more relevant for a classification of signal events. It is demonstrated, that NHB is the background most likely to mimic signal behavior over a wide range of parameters. Contrarily, the dominance of PMB must first be tackled and shows the necessity of the veto cuts. In contrast, the extended veto cuts are superfluous and the  $\nu_\mu$ -CC DIS selection cuts can be reduced in lieu of one of the presented analysis methods built around the set of discriminating parameters. The limitations on the data comparison due to the lack of run data presents a problem. On the other hand, the lack of MC statistics can be overcome to improve the performance evaluation. With this, the presented work successfully proves the feasibility of signal classification given the analysis methods with preliminary efficiencies promising to match or surpass that of the previously used selection cut strategy.

## References

- [1] Yeong Gyun Kim. A scattering and neutrino detector at the lhc (snd@lhc). Presented at the 24th International Workshop on Neutrinos From Accelerators (NuFact 2023), Seoul National University, Korea, August 2023.
- [2] Cristovao Vilela, Martina Ferrillo, Daniele Centanni, Simona Ilieva Ilieva, and Antonia Di Crescenzo. Observation of muon neutrino interactions at SND@LHC. 2023.
- [3] Daniele Centanni. A new scattering and neutrino detector at the lhc (snd@lhc). page 072, 10 2023.
- [4] SND@LHC Collaboration. Snd@lhc - scattering and neutrino detector at the lhc. Technical report, CERN, Geneva, 2021.
- [5] S. Ilieva. Measurement of the muon flux at the snd@lhc experiment. *Eur. Phys. J. C*, 84(1):90, 2024.
- [6] G. Battistoni et al. Overview of the fluka code. *Annals of Nuclear Energy*, 82:10–18, 2015. Joint International Conference on Supercomputing in Nuclear Applications and Monte Carlo 2013, SNA + MC 2013. Pluri- and Trans-disciplinarity, Towards New Modeling and Numerical Simulation Paradigms.
- [7] S. Agostinelli et al. Geant4—a simulation toolkit. *Nuclear Instruments and Methods in Physics Research Section A: Accelerators, Spectrometers, Detectors and Associated Equipment*, 506(3):250–303, 2003.
- [8] C. Andreopoulos et al. The GENIE Neutrino Monte Carlo Generator. *Nucl. Instrum. Meth. A*, 614:87–104, 2010.
- [9] Torbjorn Sjostrand, Stephen Mrenna, and Peter Z. Skands. PYTHIA 6.4 Physics and Manual. *JHEP*, 05:026, 2006.
- [10] A. Conaboy. Timing performance studies of the hadronic calorimeter of the scattering and neutrino detector at the lhc and its potential in neutrino species identification studies. 2025. Humboldt University of Berlin, Berlin.
- [11] Johannes Rauch and Tobias Schlüter. Genfit - a generic track-fitting toolkit. *Journal of Physics: Conference Series*, 608, 10 2014.

- [12] F. Pedregosa, G. Varoquaux, A. Gramfort, V. Michel, B. Thirion, O. Grisel, M. Blondel, P. Prettenhofer, R. Weiss, V. Dubourg, J. Vanderplas, A. Passos, D. Cournapeau, M. Brucher, M. Perrot, and E. Duchesnay. Scikit-learn: Machine learning in Python. *Journal of Machine Learning Research*, 12:2825–2830, 2011.
- [13] Tianqi Chen and Carlos Guestrin. Xgboost: A scalable tree boosting system. page 785–794, August 2016.

## List of Abbreviations

SND	Scattering Neutrino Detector
MC	Monte Carlo
CC, NC	charged-current, neutral-current
DIS	Charged-Current Deep Inelastic Scattering
PMB	Passing Muon Background
NHB	Neutral Hadron Background
US, DS	Upstream, Downstream
QDC	Charge-to-Digital Converter
POCA, DOCA	Position of Closest Approach, Distance of Closest Approach
EM	Electromagnetic
dof	Degrees of Freedom
BG	Background
LR	Likelihood Ratio
PMF	Probability Mass Function
BDT	Boosted Decision Tree
nll	negative log-likelihood
CM	Confusion Matrix
TP, TN, FP, FN	True Positive, False Positive, False Negative, False Negative
SM, BS	Standard Model, Beyond the Standard Model

## List of Figures

1	Location of the SND@LHC experiment . . . . .	1
2	SND cross-section and neutrino energy range . . . . .	2
3	Feynman diagram of a $\nu_\mu$ -CC DIS interaction . . . . .	2
4	Schematic diagram of SND detector . . . . .	3
5	ECC technique in the target system . . . . .	4
6	Distributions of hits in SciFi channels and DS bars . . . . .	10
7	Reconstructed target wall distribution . . . . .	11
8	Cut ratio for Y-barycenter . . . . .	13
9	Definitions of the hadron shower width and position in the US . . . . .	14
10	Barycenter distributions and residuals . . . . .	16

11	Distributions of $\lambda_X$ per US plane . . . . .	17
12	Distributions of $\lambda_Y$ per US plane . . . . .	18
13	Average $\lambda_{X/Y}$ per US plane . . . . .	19
14	Interaction wall dependent $\lambda_{X/Y}$ averages . . . . .	20
15	$\lambda$ distributions in the SciFi and DS . . . . .	21
16	Hadron shower azimuthal angle $\phi$ and polar angle $\theta$ distributions . . . . .	22
17	Reconstructed muon track: $\chi^2$ and residuals . . . . .	24
18	Parameter comparison between PMB and muon DIS . . . . .	26
19	Position of reconstructed muon tracks in the DS . . . . .	27
20	Azimuthal angle $\phi$ and polar angle $\theta$ of the reconstructed muon track . . . . .	28
21	Signal event reconstruction in the HCAL . . . . .	29
22	Likelihood ratios based on $\lambda_X$ distributions . . . . .	33
23	Correlation plot for $\lambda_X$ and $\lambda_Y$ . . . . .	34
24	LR test for $\lambda_Y$ and combined LR test for $\text{LR}_X \cdot \text{LR}_Y$ . . . . .	35
25	Combined LR test with cut on the polar angle . . . . .	36
26	Test of the likelihood fit procedure . . . . .	38
27	Likelihood fit test for a random composition of processes . . . . .	39
28	Residuals of the likelihood fit test . . . . .	40
29	Hit count per event in the HCAL . . . . .	42
30	BDT parameters . . . . .	43
31	Confusion matrix description . . . . .	44
32	Unweighted CM and loss function of the BDT . . . . .	45
33	Unweighted classification report . . . . .	46
34	Weighted CM and classification report . . . . .	47
35	BDT feature importance . . . . .	48
36	Data comparison of hadron shower position per US plane . . . . .	52
37	Histogram entry count for MC and run data . . . . .	52
38	Data comparison of hadron shower width per US plane . . . . .	53
39	Average $\lambda$ values for MC and run data per US plane . . . . .	54
40	Likelihood fit procedure applied to run data . . . . .	55
41	Cut ratio for Y-Barycenter . . . . .	65
42	Distribution of cut ratio for $\lambda_X$ . . . . .	65
43	Distributions of cut ratio for $\lambda_Y$ . . . . .	66

44	LR test for the SciFi hit count and polar angle of the reconstructed muon track	66
45	Likelihood fit test for $\lambda_Y$ . . . . .	67
46	LR test performed on run data . . . . .	67

## List of Tables

1	Expected yield of NHB per energy range . . . . .	7
2	Selection cut efficiencies for signal and background processes . . . . .	9

## A Figures

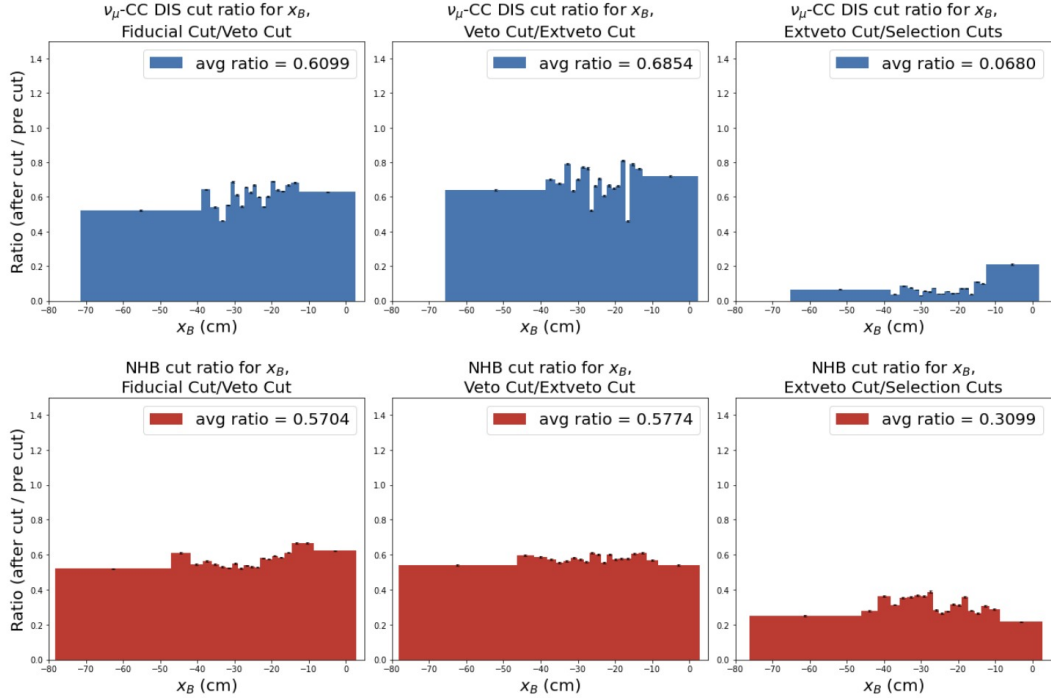


**Figure 41:** Cut ratios for select cuts for the barycenter  $x_B$  in X. A constant cut ratio indicates the shape of the distribution isn't heavily influenced by the cut.

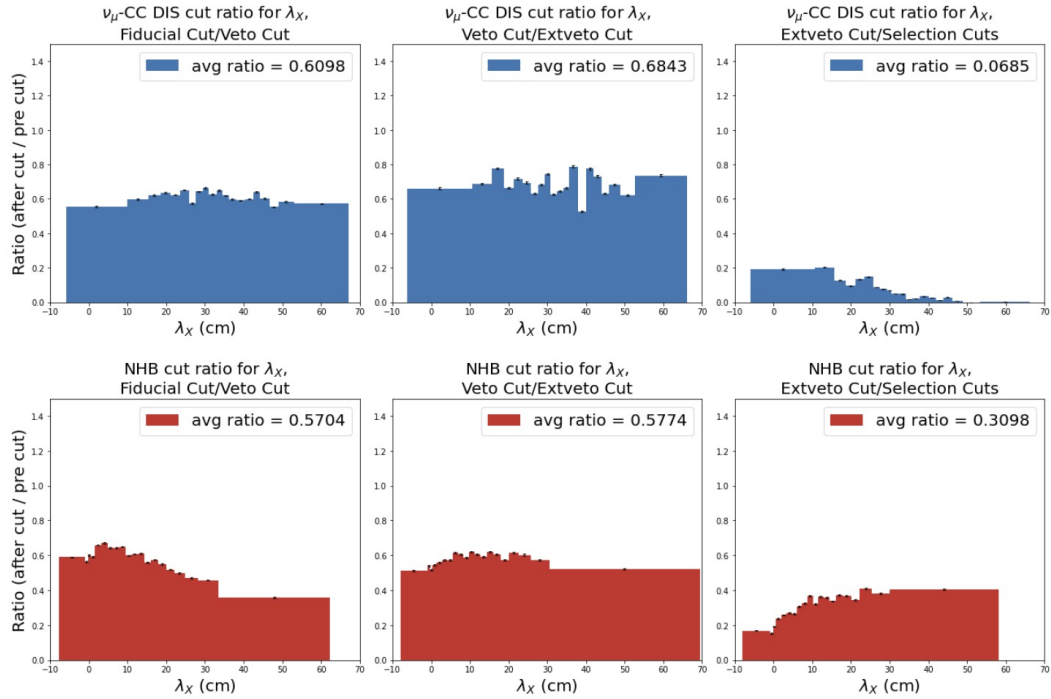


**Figure 42:** Depicted are the cut ratios of the  $\lambda_X$  distributions before and after the following cuts: veto cut, extended veto cuts, selection cuts.

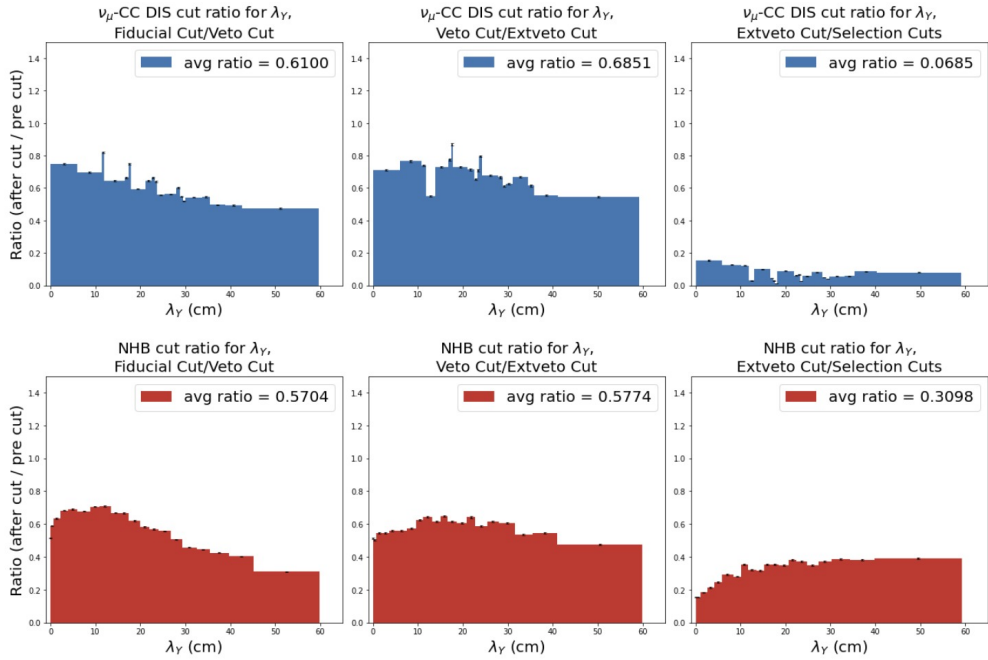


**Figure 43:** Ratios of the  $\lambda_Y$  distributions before and after select cuts quantify how much the shape of these distributions are affected by the cuts.

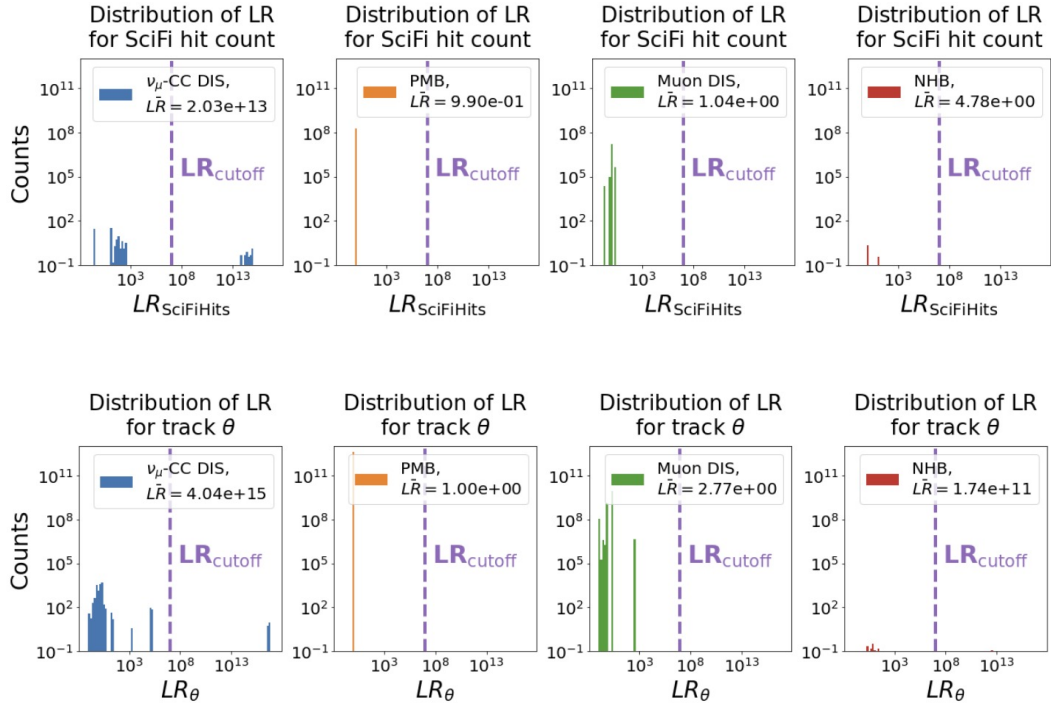


**Figure 44:** Likelihood ratio test for the hit count per event in the SciFi (top) and the polar angle of the reconstructed muon track  $\theta$  (bottom). A cutoff value of  $10^7$  is applied and 4.3% of the statistics pass this cutoff for the SciFi hit count and 0.7% for the polar angle.

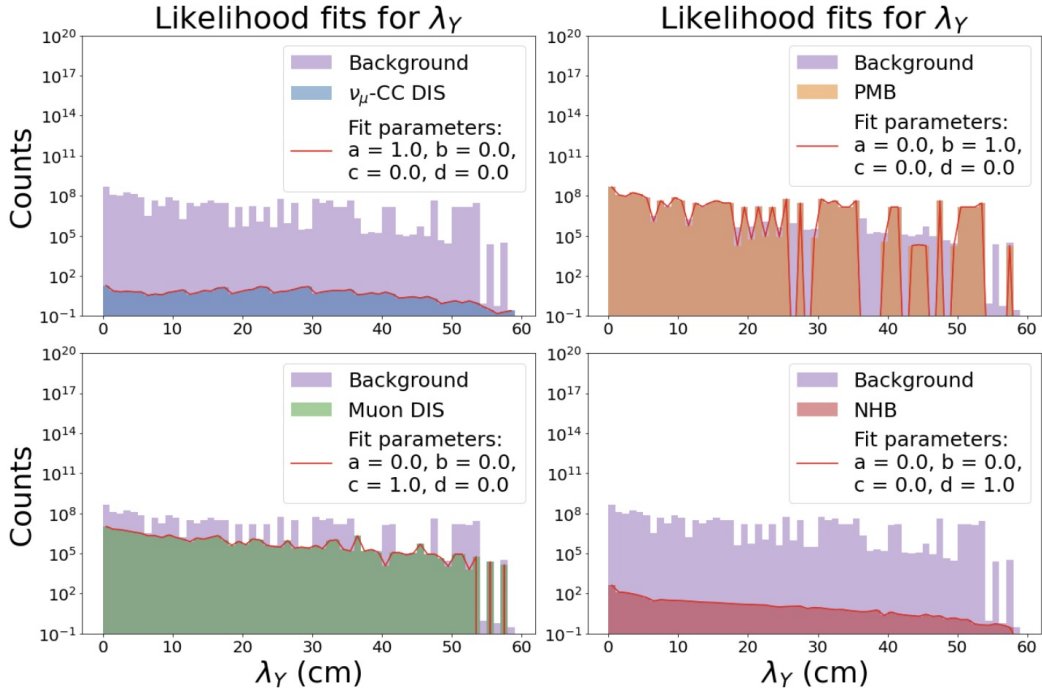


**Figure 45:** In an initial test for  $\lambda_Y$  the fitting procedure is tested on the trivial case of identifying each of the four processes. The fit parameters  $a, b, c, d$  accurately represent the contribution of each process.

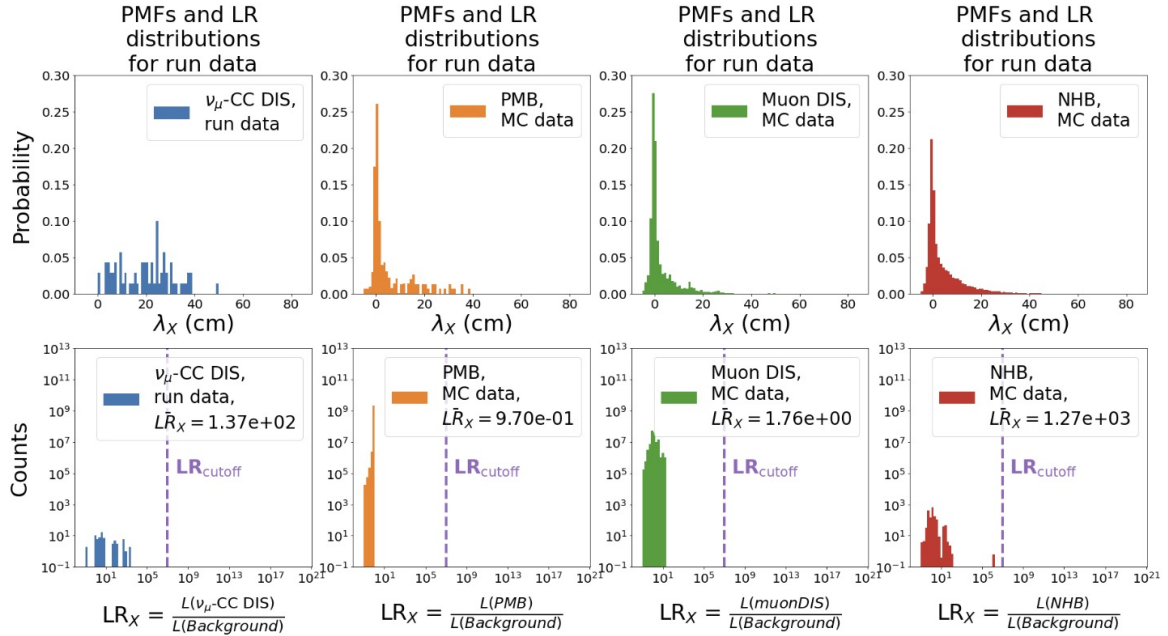


**Figure 46:** PMFs (top) and LR (bottom) distributions for signal run data in blue and background MC data. The same cutoff value of  $10^7$  is applied as in chapter 4.1.1.